Photoredox Catalysis Driven by Visible Light and Iron N-Heterocyclic Carbene Complexes

de Groot, Lisa

2023

Document Version:
Publisher's PDF, also known as Version of record

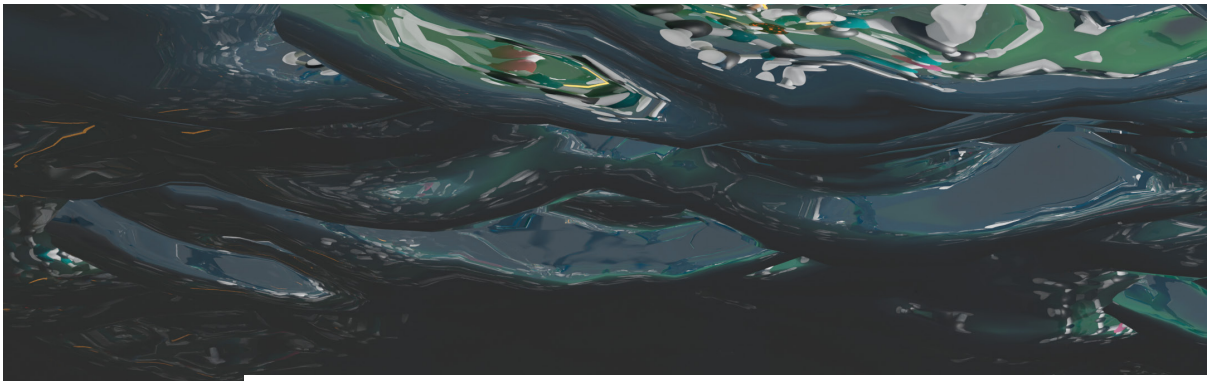

Photoredox Catalysis Driven by Visible Light and Iron *N*-Heterocyclic Carbene Complexes

LISA H. M. DE GROOT | CENTRE FOR ANALYSIS AND SYNTHESIS | LUND UNIVERSITY

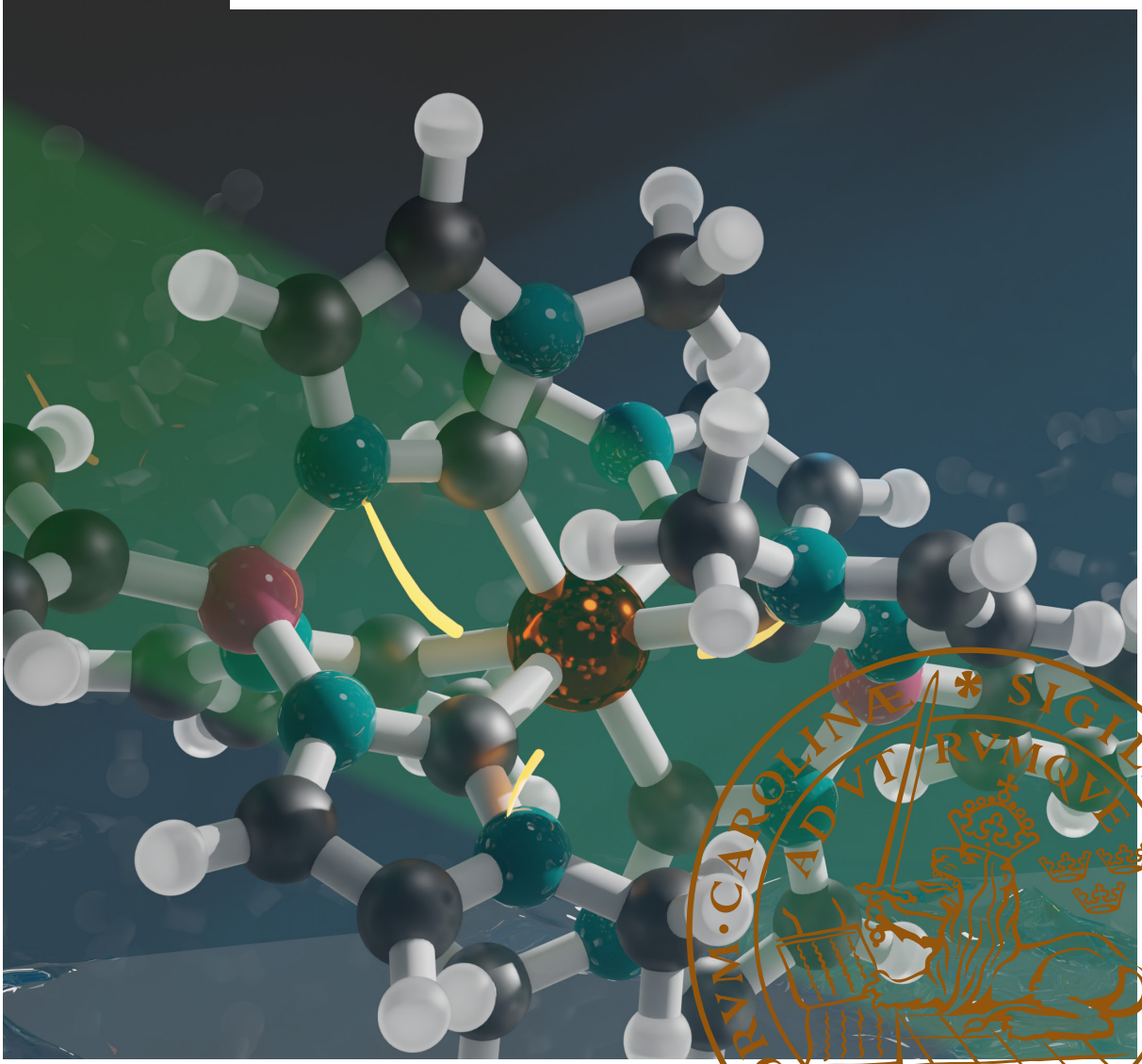

Photoredox Catalysis Driven by Visible Light and Iron *N*-Heterocyclic Carbene Complexes

Photoredox Catalysis Driven by Visible Light and Iron *N*-Heterocyclic Carbene Complexes

Lisa H. M. de Groot

LUND
UNIVERSITY

DOCTORAL DISSERTATION

Doctoral dissertation for the degree of Doctor of Philosophy (PhD) at the Faculty of Science at Lund University to be publicly defended on the 8th of December at 09.00 in lecture hall C, A-Huset (LTH), Sölvegatan 24, 223 62 Lund

Faculty opponent
Assoc. Prof. Markus D. Kärkäs (Kungliga Tekniska högskolan (KTH), Sweden)

Organization: LUND UNIVERSITY, Faculty of Science, Department of Chemistry

Document name: Doctoral Dissertation **Date of issue:** 2023-12-08

Author(s): Lisa H. M. de Groot **Sponsoring organization:**

Title and subtitle: Photoredox Catalysis Driven by Visible Light and Iron *N*-Heterocyclic Carbene Complexes

Abstract:

Photoredox catalysis is a rapidly expanding field, in which organic transformations are catalysed using light. The most commonly used photoredox catalysts (PCs) are transition metal complexes which absorb in the visible region of the electromagnetic spectrum. Traditionally, such PCs are based on scarce and expensive metals, such as ruthenium or iridium, in combination with polypyridyl ligands. Research has been dedicated to replacing these metals with the Earth-abundant metal iron. However, iron polypyridyl complexes exhibit poor excited state (ES) lifetimes on the sub-picosecond timescale, which significantly limits their use as PCs.

Replacing the polypyridyl ligands with strongly σ-donating *N*-heterocyclic carbene (NHC) ligands, has led to Fe-NHC complexes which posess charge-transfer ESs with longer lifetimes on the picosecond to nanosecond timescale. Furthermore, these complexes exhibit beneficial ES reduction and oxidation potentials. An additional benefit of these Fe-NHCs, is that they absorb in the green region of the visible spectrum, which is of lower energy than the commonly employed blue light. The use of such low energy light not only requires less energy, but can also potentially avoid undesireable side-reactions.

The applicability of three different Fe-NHC complexes as PCs utilising green light has been probed by their application on two different organic reactions: the atom transfer radical addition (ATRA) reaction, and the base-promoted homolytic aromatic substitution (BHAS) reaction.

Firstly, the application of Fe-NHC complexes on the ATRA reaction was investigated, in which several photoreactors were assessed. Reaction optimisations were performed and extensive mechanistic investigations were conducted, which included a variety of methods grounded in organic synthetic chemistry and physical chemistry. Interestingly, an Fe-NHC complex was found to efficiently catalyse the ATRA reaction via a reductive quenching cycle, utilising a consecutive photoinduced electron transfer in which both the Fe(III) and Fe(II) oxidation states of the complex were involved. Furthermore, the reaction was also found to proceed in absence of a sacrificial electron donor, utilising the Fe(III)-NHC PC in an oxidative quenching cycle. Lastly, a broad substrate scope was established.

Similarly, the use of Fe-NHC complexes to catalyse the BHAS reaction was examined. This reaction was found to be catalysed by an Fe(III)-NHC PC under green light irradiation. The reaction conditions were optimised and a substrate scope was established. Also in this case, mechanistic investigations were conducted.

This thesis aims to contribute to the field of iron photoredox catalysis, employing charge-transfer ESs to efficiently catalyse organic transformations under irradiation with green light.

Key words: Photoredox catalysis, iron *N*-heterocyclic carbene complexes, visible light, ATRA, BHAS

Classification system and/or index terms (if any) Supplementary bibliographical information

Language English **ISSN and key title**:

ISBN: 978-91-8096-000-7 (printed), 978-91-8096-001-4 (digital)

Recipient's notes **Number of pages**: 83

Price Security classification

Signature Date 2023-10-23

Photoredox Catalysis Driven by Visible Light and Iron *N*-Heterocyclic Carbene Complexes

Lisa H. M. de Groot

LUND
UNIVERSITY

Front cover: illustration by Tommy Dam
Back cover: photograph of the TAK120 photoreactor setup by Lisa H. M. de Groot

Faculty of Science
Department of Chemistry
Centre for Analysis and Synthesis

ISBN 978-91-8096-000-7 (printed)
ISBN 978-91-8096-001-4 (digital)

Printed in Sweden by Media-Tryck, Lund University
Lund 2023

I have not failed 10,000 times. I have not failed once. I have succeeded in proving that those 10,000 ways will not work. When I have eliminated the ways that will not work, I will find the way that will work.

– Thomas A. Edison

Table of contents

Popular science summary

Chemical reactions usually involve the breaking and formation of bonds between atoms of the chemicals involved in a reaction and can for example be used to produce pharmaceuticals. When a reaction is catalysed, in other words enabled or sped up, a molecule is used which is called a catalyst and is not consumed during the reaction. In this thesis, the focus is on catalysts which are able to capture energy from light and use it to catalyse organic reactions. Especially catalysts which absorb visible light are of interest, since that is where the solar irradiance is highest.

Metal complexes are commonly used as photocatalysts. These are compounds that consist of a metal centre to which ligands, usually organic compounds, are coordinated. The combination of a specific metal with its connected ligands influences which properties the catalyst possesses, for example which colour it absorbs and which reactions it can catalyse. Photocatalysts usually contain metals that are scarce and expensive, such as ruthenium or iridium. For comparison, gold is forty times more abundant than iridium in the Earth's crust.

Therefore, there has been much research dedicated to finding new photocatalysts which are based on more Earth-abundant metals. Iron is one of the most abundant metals in the Earth's crust. However, changing a metal centre in a metal complex from ruthenium or iridium to iron also greatly influences the properties of the whole molecule. Replacing the core metal with iron, keeping the same ligands as used previously with ruthenium or iridium, does not lead to the properties which are desired in a well-functioning photocatalyst. Therefore, alternative ligands have been investigated to acquire iron complexes with more beneficial properties.

Photocatalysts usually work by using the energy of the light it captures to push an electron present in the molecule to a higher energy level, leaving a hole in the energy level from where the electron originated. Subsequently, two different processes can occur. The high energy electron can be donated to the compound which is involved in the chemical reaction (usually called a substrate). Alternatively, the hole can be filled by an electron from the substrate. The compound which donates an electron is oxidised in the process, whereas the compound that accepts the electron is reduced. The overall process is often referred to as a redox (red = reduction, ox = oxidation) reaction. Photocatalysts that use redox processes in combination with light are therefore often called photoredox catalysts (PCs).

In this thesis, the use of new iron complexes as PCs has been investigated on two different chemical reactions: the atom transfer radical addition (ATRA) reaction and the base-promoted homolytic aromatic substitution (BHAS) reaction.

List of papers

This thesis summarises and supplements the following papers:

I. Photoredox catalysis *via* consecutive ^{2}LMCT- and ^{3}MLCT-excitation of an Fe(III/II)–N-heterocyclic carbene complex

Aleksandra Ilic, Jesper Schwarz, Catherine Johnson, **Lisa H. M. de Groot**, Simon Kaufhold, Reiner Lomoth and Kenneth Wärnmark

Chem. Sci., 2022, **13**, 9165–9175.

II. Base-promoted homolytic aromatic substitution (BHAS) reactions and hydrodehalogenations driven by green light and an iron(III)-NHC photoredox catalyst

Lisa H.M. de Groot, Valtýr Freyr Hlynsson, Catherine Johnson, Alpesh K. Sharma, Reiner Lomoth and Kenneth Wärnmark

In manuscript

List of papers not included in this thesis:

III. HERFD-XANES probes of electronic structures of iron$^{II/III}$ carbene complexes

Meiyuan Guo, Om Prakash, Hao Fan, **Lisa H. M. de Groot**, Valtýr Freyr Hlynsson, Simon Kaufhold, Olga Gordivska, Nicolás Velásquez, Pavel Chabera, Pieter Glatzel, Kenneth Wärnmark, Petter Persson and Jens Uhlig

Phys. Chem. Chem. Phys., 2020, **22**, 9067–9073.

IV. Iron Photoredox Catalysis–Past, Present, and Future

Lisa H. M. de Groot, Aleksandra Ilic, Jesper Schwarz and Kenneth Wärnmark

J. Am. Chem. Soc., 2023, **145**, 9369–9388.

Author's contribution to the papers

Paper I

I conceived the project and performed the early testing, data collection and optimisations of various reactions and photoreactor setups. I contributed to the revision of the manuscript.

Paper II

I performed large parts of the experimental work, including reaction optimisations, defining the substrate scope and product isolations. I planned and carried out part of the mechanistic investigations such as radical trapping experiments and chemical actinometry. I conceived the proposed mechanisms, wrote major parts of the entire manuscript, and coordinated the writing.

Paper III

I have provided compounds for X-ray studies.

Paper IV

I drafted and revised the manuscript together with the other co-authors and coordinated the writing.

Abbreviations

A	Electron acceptor
AP	Aldehyde side-product
btz	4,4'-Bis(1,2,3-triazol-5-ylidene)
^{t}BuOK	Potassium *tert*-butoxide
conPET	Consecutive photo-induced electron transfer
CNC	2,6-Bis(3-methylimidazole-1-ylidine)pyridine
CP	Cyclised product
D	Electron donor
DCM	Dichloromethane
DMA	*N*,*N*-Dimethylaniline
EA	Elemental analysis
ES	Excited state
EtOAc	Ethyl acetate
FA	Formic acid
GS	Ground state
HMQC	Heteronuclear multiple quantum coherence
HP	Hydrogen addition product (also: hydrodehalogenated product or dehalogenated product)
IS	Internal standard
LC	Ligand centred
MC	Metal centred
PC	Photoredox catalyst
PE	Petroleum ether
phtmeimb	Phenyl(tris(3-methylimidazol-2-ylidene))borate
PS	Photosensitiser
SED	Sacrificial electron donor
SET	Single electron transfer
SPE	Solid-phase extraction

TA	Transient absorption
TEA	Triethylamine
TM	Transition metal
TMP	2,2,6,6-Tetramethylpiperidine
TON	Turnover number
XAT	Halogen atom transfer

Abbreviations found in the ACS style guide are not included in this list.

1 Introduction

1.1 Visible light photoredox catalysis

In the rapidly expanding field of photocatalysis, chemical transformations are driven by light.[1–4] The utilisation of light for the activation of molecules has enabled the discovery of new reactivity as well as the improvement of many previously established reactions.[1–4] Organic transformations that are being catalysed by visible light are of particular interest because that part of the solar spectrum exhibits the highest irradiance.[4] Furthermore, the use of such low energy light potentially counteracts undesired side-reactions that could be the result of traditional harsh reaction conditions such as heating or microwave irradiation, or the employment of high energy ultraviolet (UV) light.[1–4]

Photoredox catalysis is a branch of photocatalysis in which single electron transfer (SET) is utilised to activate reaction components and generate radical intermediates in a controlled manner.[1–3] A photosensitiser (PS) (also known as dye or chromophore) or photoredox catalyst (PC) can be employed to capture the photon energy.[3,5] In this thesis, the focus will be on PCs — PSs which exhibit photoredox catalytic reactivity.

Scheme 1 illustrates the typical mode of action of photoredox catalysis.[1,2,5] Upon irradiation of a PC, an electron is promoted from the ground state (GS) to an excited state (ES). The PC in its ES (*PC) can consequently partake in SET with an electron donor (D) or acceptor (A). D or A can be a sacrificial reaction component, a substrate (S), or a reactive intermediate. In the reductive quenching pathway, the *PC is reduced by D, whereas oxidation of the *PC by A is referred to as oxidative quenching. This process generates the GS of the PC in another oxidation state. In order to close the catalytic cycle, the PC needs to participate in SET once more with a reaction intermediate, substrate, or a sacrificial reductant or oxidant. This restores the PC to its original oxidation state.[1,2,5]

The efficiency and thermodynamic driving force of the beforementioned steps determine in part the efficiency of the overall photoredox catalytic reaction. PCs should therefore ideally be designed and optimised keeping the following key properties in mind: 1) They should exhibit significant absorption of visible light (high ε (molar absorption or extinction coefficient)), ideally in a region where other reaction components do not absorb. This will optimise the initial photoexcitation

from the GS to the ES and prevent undesired side-reactions. 2) They should possess ES lifetimes that are long enough (preferably in the ns–µs range) to participate in productive bimolecular quenching with an electron donor or acceptor. 3) Their ESs should possess favourable redox potentials to provide a significant driving force for the SET involved in bimolecular quenching. Furthermore, the redox process needs to be reversible to prevent degradation of the PC upon reduction or oxidation. 4) They should be sufficiently photostable, to allow for photoredox catalysis with high turnover numbers (TON).[6]

All the beforementioned properties complement each other, and as a whole, they play an important role in the efficiency and utility of PCs.

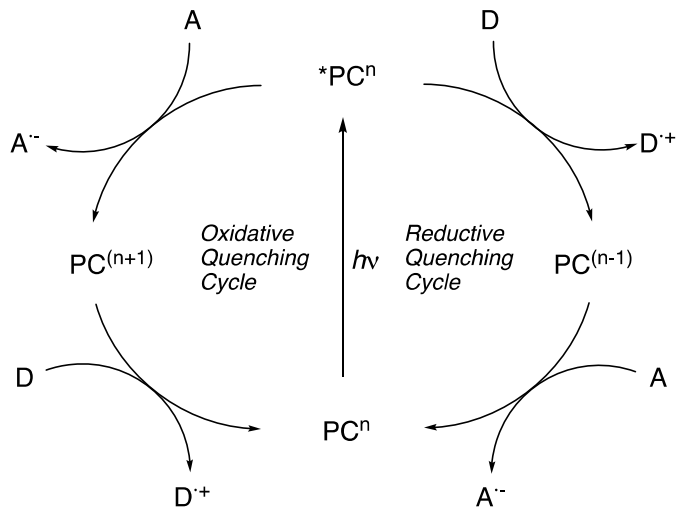

Scheme 1. A schematic overview of a photoredox catalytic cycle for oxidative and reductive quenching cycles. PC = photoredox catalyst, D = electron donor, A = electron acceptor.

1.2 Photophysics of photoredox catalytic processes

Gaining insight into the photophysical processes involved in photoredox catalytic reactions is valuable for their development and improvement. The different steps that are involved in photoredox catalytic processes are described in more detail in Scheme 2.[7,8] In the initial step, the PC is excited by light to generate the *PC (the ES). The efficiency of this step is mostly dependent on the absorption wavelength (λ_{abs}), and extinction coefficient (ε_{max}) of the PC at the excitation wavelength. In the absence of any other reaction component which can quench the *PC (in other words, accept from or donate an electron to the *PC), it will decay back to the GS via radiative (k_r) and nonradiative decay (k_{nr}). If a quencher (Q) is present (in Scheme

2, a reductive quencher is provided), the *PC can participate in non-radiative energy transfer (Förster or Dexter energy transfer) or, more commonly, SET. In the case of the latter, reductive quenching generates the reduced PC in the GS and the oxidised Q (or the oxidised PC and reduced Q if an oxidative quenching mechanism is operative). Again, Q can be sacrificial in nature, or a substrate or other reaction intermediate. For efficient photoredox catalysis, the rate (k_q) and efficiency (η_q) of quenching play a major role. Furthermore, the ES lifetime of the *PC needs to be sufficiently long to allow for bimolecular quenching. Once the quenching has taken place, the two components are still in close proximity to each other within the solvent cage. Here, either unproductive back-combination (k_{bc}), or cage escape (k_{ce}) can take place. The cage escape yield (η_{ce}) indicates to which extent cage escape is favoured over back-combination, and hence how efficiently the charge separated components escape the solvent cage. After cage escape, unproductive back-donation (k_{bd}) can take place which regenerates the PC and Q, or the reduced PC can undergo SET with a substrate (S) (k_s). The overall quantum yield of the number of photons that are absorbed by the system to generate PC^{-} is defined as $\Phi = \eta_q\eta_{ce}$. From this equation one can deduce that it is not only the quenching of the ES, but also the cage escape yield that plays an important role in the overall efficiency of the photoredox catalytic process.[7,8]

(1)	$PC + h\nu \rightarrow {}^{*}PC$	
(2)	$^{*}PC \rightarrow PC + h\nu$	k_r
(3)	$^{*}PC \rightarrow PC + \text{heat}$	k_{nr}
(4)	$^{*}PC + Q \rightarrow [PC^{-} + Q^{+}]$	k_q, η_q
(5)	$[PC^{-} + Q^{+}] \rightarrow PC + Q$	k_{bc}
(6)	$[PC^{-} + Q^{+}] \rightarrow PC^{-} + Q^{+}$	k_{ce}, η_{ce}
(7)	$PC^{-} + Q^{+} \rightarrow PC + Q$	k_{bd}
(8)	$PC^{-} + S \rightarrow PC + S^{-}$	k_s

Scheme 2. An overview of the different steps that commonly occur upon excitation of a photoredox catalyst (PC) by light. In this case, reductive quenching of the excited state (ES) is illustrated. Q = quencher, S = substrate, k_r = rate of radiative decay, k_{nr} = rate of nonradiative decay, k_q = rate of quenching, η_q = quenching yield, k_{bc} = rate of back-combination, k_{ce} = rate of cage escape, η_{ce} = cage escape yield, k_{bd} = rate of back-donation, k_s = rate of single electron transfer (SET) to the substrate. Adapted from ref. 8.

1.3 Investigating photoredox catalytic mechanisms

1.3.1 Physical chemistry methods

Determining the photophysical properties of the different components involved in photoredox catalysis can be of great benefit to not only gain more insight into the photoredox catalytic mechanism at play, but also to determine which reaction components can be combined to lead to efficient photoredox reactivity.

Steady-state absorption spectroscopy (also commonly referred to as UV-Vis or electronic absorption spectroscopy) can be employed to determine the extinction coefficient (ε_{max}) and absorption maxima (λ_{abs}) for a PC.[6] The observed absorption bands can be assigned to different electronic transitions, such as LC (ligand centred), MC (metal centred), LMCT (ligand-to-metal charge-transfer) or MLCT (metal-to-ligand charge-transfer) transitions.[9]

The absorption spectroscopy can be complemented by emission spectroscopy to calculate the difference in energy between the ground state (GS) and the excited state (ES) from which emission takes place.[6] The emission quantum yield (Φ) provides a the ratio of the number of photons emitted by the system during non-radiative decay, versus the amount of photons used for the photoexcitation. The obtained absorption and emission data can be complemented with density functional theory (DFT) calculations to support the assignment of the absorption and emission features to different transitions between electronic states.[10] Absorption spectroscopy can also be employed to probe the photostability of a PC, as different absorption features will appear or disappear upon degradation.[10]

Time-resolved spectroscopy, such as transient absorption (TA) spectroscopy and time-resolved emission spectroscopy can be employed to determine ES lifetimes of PCs in different solvents, as well as the types of ESs (for example charge-transfer or metal centred ESs) accessible for the PC.[6]

Spectroscopic techniques can also be used to provide valuable insights on the rates and efficiency of the different electron transfer processes. For example, the decrease in emission (radiative decay) of the ES in presence of Q (in varying concentrations), can be measured spectroscopically. The obtained luminescence quenching data is subjected to a Stern–Volmer analysis, allowing the quenching rate (k_q) of the ES by a certain Q to be determined. This analysis can be performed for a range of potential Qs or PCs, in a variety of solvents. The data can then be used to gain mechanistic insights and/or further optimise the reaction conditions.[6]

Cyclic voltammetry (CV) is a method commonly used to determine the reduction and oxidation potentials (and their reversibility) of PCs and/or other reaction components involved in SET (for example substrates or sacrificial electron donors/acceptors).[6] This provides a facile method of determining thermodynamic feasibility of the SET between an electron donor and acceptor.[6]

Lastly, electron paramagnetic resonance (EPR) spectroscopy can be employed to probe for molecules possessing unpaired electrons (radicals) within the reaction mixture.[11] However, because EPR spectroscopy requires specialised equipment, many research groups opt for the chemical trapping of radical intermediates instead, upon which the radical adduct can be analysed.[11] This method will be discussed further in the next section.

1.3.2 Organic chemistry methods

NMR (Nuclear Magnetic Resonance) spectroscopy is commonly used within the field of synthetic organic chemistry. This method is often considered necessary to gain valuable structural information on the reaction components. Within the field of photochemistry, this method is most often used to trace the conversion of a substrate to the corresponding product over time. Yields of reactions can be determined by recording a ^{1}H NMR of an aliquot of the reaction mixture, to which a known amount of a compound (internal standard (IS)) has been added. Furthermore, the degradation of a PC can be visualised. In the latter case, NMR spectroscopy is often used complementary to UV-Vis absorption spectroscopy.

As mentioned before, radical trapping can be used to prove radical mechanisms and is an often more accessible alternative to EPR spectroscopy.[12] The radical trap is added to the reaction mixture and can react with radical intermediates, preventing them from participating further in radical reactions. If the product formation is completely or partially hampered (usually shown by ^{1}H NMR spectroscopy), this indicates the presence of a radical pathway. Furthermore, ^{1}H NMR spectroscopy or mass spectrometry (MS), can be used to identify adducts of the radical trap and radical reaction intermediates.[12]

Together, all of the beforementioned methods can be used to elucidate photoredox catalytic mechanisms and aid in the discovery of novel reactivity.

1.4 Chemical structure of photoredox catalysts

1.4.1 Traditional photoredox catalysts

Over the last decades, a wide variety of new PCs have been designed and successfully applied to organic transformations.[13] Two of the most commonly found classes of PCs are either 1) organic compounds that contain aromatic moieties,[5,14] such as Eosin Y[15] (**1**) (Figure 1), or, more commonly, 2) transition metal (TM) complexes. Due to the rather facile tuneability of TM-complexes by exchange of the core metal or adaptation of the attached ligand(s), these are commonly investigated as potential PCs. Many traditional PCs based on TM-complexes

contain rare metals, such as ruthenium[2] (**2**) or iridium[16] (**3**) (Figure 1). Their photophysical properties have been thoroughly investigated and these types of PCs are well established within the field of photoredox catalysis. However, as the name implies, these metals are scarce, and therefore there is an increasing interest for discovering functional TM-PCs based on more Earth-abundant metals. This has led to an increase in reports on the successful use of PCs based on metals such as copper[17] (**4**), molybdenum[18] (**5**) and tungsten[19] (**6**) (Figure 1).[1,20]

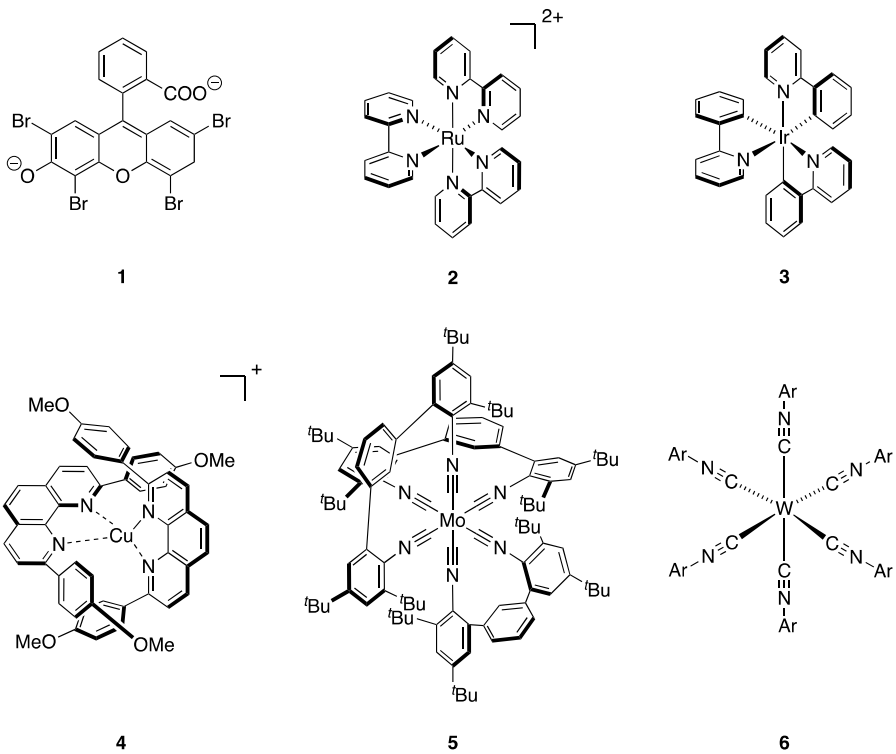

Figure 1. Selected examples of known photoredox catalysts (PCs). Ar = diisopropylphenyl moiety featuring varying substituents.

1.4.2 Photoredox catalysts based on iron

Being the most Earth-abundant of all TMs, iron is yet another attractive alternative to scarce metals. However, iron complexes that resemble their ruthenium or iridium counterparts (commonly polypyridyl complexes), suffer short, sub-picosecond ES lifetimes and are therefore generally not useful as PCs.[21]

To explain why iron polypyridyl complexes exhibit poor ES lifetimes compared to their ruthenium analogues, the excitation and deactivation pathways present for the different complexes need to be addressed. Inherent differences can be observed

between the d-orbital splitting found in ruthenium as compared to iron polypyridyl complexes (Figure 2). Although metal complexes which possess bi- or tridentate ligands generally do not exhibit a perfectly octahedral geometry, the d orbitals have been labelled t_{2g} and e_g^* and are ordered as if they were present in a perfect octahedral ligand field, for the sake of clarity. Polypyridyl ligands, such as bipyridine (bpy), are strong-field ligands, which results in both $[Ru(II)\text{-}(bpy)_3]^{2+}$ and $[Fe(II)\text{-}(bpy)_3]^{2+}$ being low-spin d^6-complexes. The improved metal–ligand interactions found in the 4d Ru(II) complex, as compared to its 1st row TM Fe(II) counterpart, causes the e_g^* orbital set to be higher in energy than the ligand-based π^*, making the ligand-based π^* the lowest unoccupied molecular orbital (LUMO). For an Fe(II) polypyridyl complex, the ligand field splitting of the d-orbitals is smaller, which leads to the metal-based e_g^* orbitals being the LUMO instead. For both ruthenium and iron polypyridyl complexes, the t_{2g} is the highest occupied molecular orbital (HOMO), which exhibits predominantly metal character.[21]

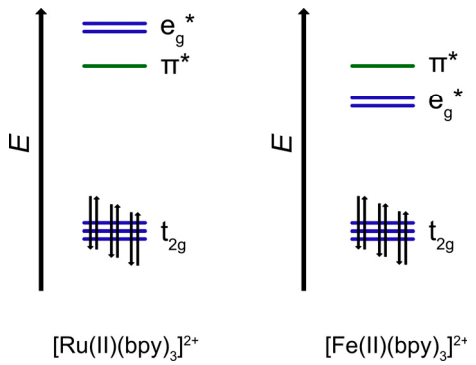

Figure 2. Schematic overview of the molecular orbital (MO) diagrams with the frontier molecular d-orbitals and ligand-based orbitals present in Ru(II) and Fe(II) polypyridyl complexes.[21]

Due to the beforementioned properties, different excitation and deactivation pathways are observed for ruthenium and iron polypyridyl complexes (Figure 3). Photoexcitation of $[Ru(II)(bpy)_3]^{2+}$ promotes an electron from the metal-based t_{2g} orbitals to the ligand-based π^* orbital, which generates a ^{1}MLCT. The ^{1}MLCT state undergoes fast intersystem crossing (ISC), i.e. a spin-flip, to the more stable ^{3}MLCT state. The ^{1}MLCT and ^{3}MLCT states are similar in energy to the ^{3}MC and ^{5}MC states, meaning that a transition from the former to the latter is not favoured. The inaccessibility of deactivation pathways via the MC states (Figure 3a, dotted lines) results in a long-lived CT state (930 ± 40 ns in deaerated acetonitrile)[6].

$[Fe(II)(bpy)_3]^{2+}$ (Figure 3b) undergoes the same type of photoexcitation as $[Ru(II)(bpy)_3]^{2+}$, and hence ^{1}MLCT and ^{3}MLCT states are observed for this complex as well. However, due to the lower-lying metal-based e_g^* orbitals, fast radiationless decay to the GS on the sub-picosecond timescale via the ^{3}MC and ^{5}MC states is

facilitated. Therefore, this complex exhibits a short-lived CT-ES (<100 fs in acetonitrile).[22]

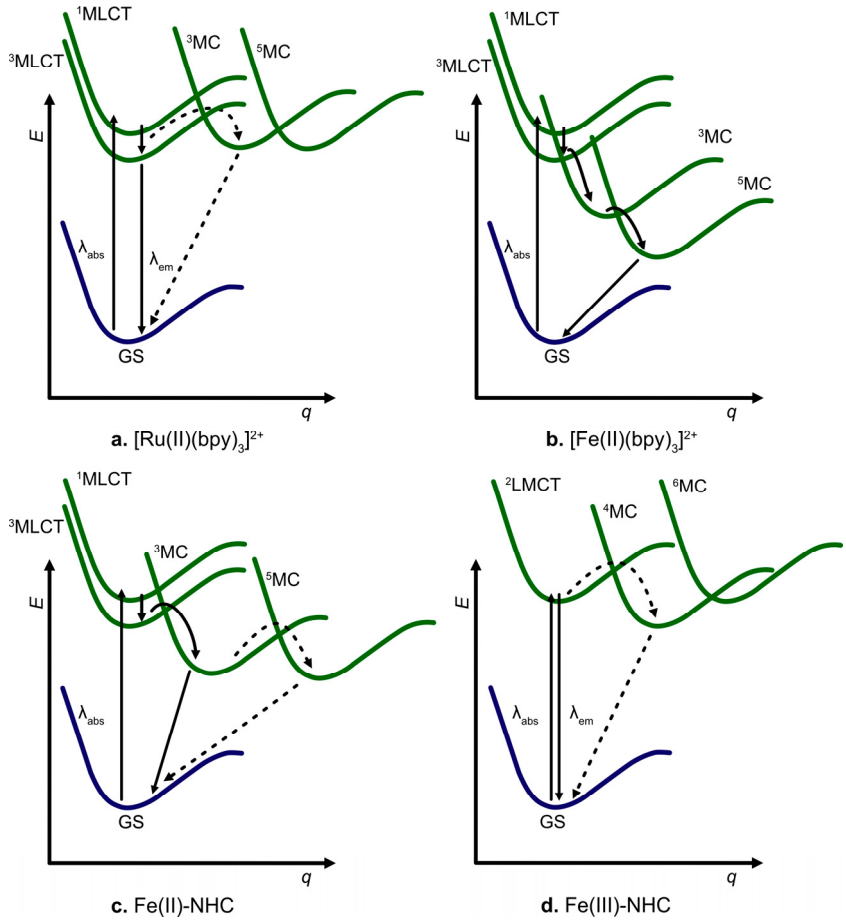

Figure 3. An overview of the different energy transitions found in ruthenium and iron polypyridyl complexes as compared to those found in Fe(II)- and Fe(III)-NHC complexes. *q* = reaction coordinate.

To hamper this fast deactivation pathway, the low-lying e_g^* orbitals can be raised in energy, which in turn raises the ^{3}MC and ^{5}MC states in energy. Such an effect can be achieved by the exchange of polypyridyl ligands for strongly σ-donating *N*-heterocyclic carbene (NHC) ligands.[21,23–26] In Fe(II)-NHC complexes (Figure 3c), for example $[Fe(CNC)_2](PF_6)_2$ (CNC = 2,6-bis(3-methylimidazole-1-ylidine)pyridine),[23,26] the transition from the ^{3}MLCT to the ^{3}MC state is generally accessible, albeit via a slight energy barrier going from the former to the latter.[23] The ^{5}MC state is similar in energy to the ^{3}MC state, but as the geometry of the complex in the ^{5}MC state is significantly different from the GS geometry, the ^{5}MC state is pushed further to the right on the

reaction coordinate (q), making it inaccessible (Figure 3c, dotted line). Therefore, the deactivation pathway mainly proceeds via the ^{3}MC state to the GS (Figure 3c, solid line).[23] This gives this Fe(II)-NHC complex an ES lifetime of approx. 9 ps,[23] which is significantly longer than the observed ES lifetimes for iron polypyridyl complexes. In the case of some Fe-NHC complexes, the σ-donation is so strong, that the oxidation state of the complex changes from Fe(II) to Fe(III) under ambient conditions.[10,27] For those complexes, only five d-electrons are present, which allows for an excitation from the ligand-based π orbitals to the metal-based t_{2g} orbitals, generating rather long-lived ^{2}LMCT states (Figure 3d and Figure 4) which decay on the pico-[27,28] and nanosecond[10] timescale. For Fe(III)-NHC complexes, the ^{4}MC and ^{6}MC states are comparatively high in energy, and therefore less accessible to allow for fast deactivation (Figure 3d, dotted lines).[10,21,24,29]

Some of the most promising Fe-NHC complexes feature strongly σ-donating ligands such as the bidentate mesoionic btz (4,4'-bis(1,2,3-triazol-5-ylidene)) or the tridentate scorpionate (tripodal) phtmeimb (phenyl(tris(3-methylimidazol-2-ylidene))borate) ligand. The Fe-NHC complexes $[Fe(II)(btz)_3](PF_6)_2$ (**7**), $[Fe(III)(btz)_3](PF_6)_3$ (**8**) and $[Fe(III)(phtmeimb)_2](PF_6)$ (**9**) (Figure 5) feature ES lifetimes of 528 ps (^{3}MLCT),[28] 100 ps (^{2}LMCT) [27] and 2 ns (^{2}LMCT),[10] respectively. Furthermore, these Fe-NHC complexes possess favourable redox potentials in their ESs (Figure 5), and feature absorption maxima in the green region of the visible spectrum, whereas many traditional PCs feature absorption maxima in the higher energy blue region. These properties make **7**, **8** and **9** excellent candidates for further exploration of their use as PCs.

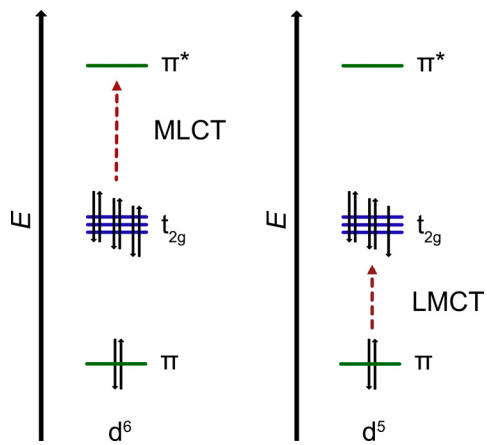

Figure 4. Schematic overview of the d orbitals and ligand orbitals, showing the metal-to-ligand charge-transfer (MLCT) and ligand-to-metal charge-transfer (LMCT) electronic transitions found in Fe(II)-NHC (d^6) and Fe(III)-NHC (d^5) complexes, respectively.[21]

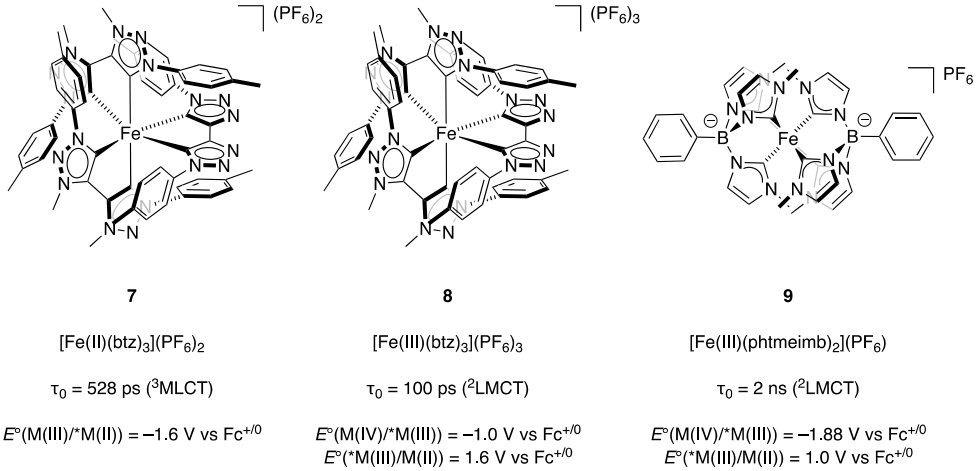

Figure 5. Structures of Fe-NHC complexes $[Fe(II)(btz)_3](PF_6)_2$ [28] (**7**), $[Fe(III)(btz)_3](PF_6)_3$ [27] (**8**) and $[Fe(III)(phtmeimb)_2](PF_6)$ [10] (**9**) with their corresponding excited state (ES) lifetimes and redox potentials.

1.5 Aim of this thesis

This thesis aims to explore the utility of iron *N*-heterocyclic carbene complexes as novel photoredox catalysts (PCs) under visible light irradiation with green light. Previously established PCs are generally TM complexes based on scarce metals, such as ruthenium and iridium. However, continued efforts have been made to discover new Earth-abundant transition metal complexes which exhibit similarly beneficial properties.

Due to their prolonged excited state lifetimes, visible light absorption, and beneficial redox potentials, it was hypothesised that Fe-NHC complexes **7**, **8** and **9** could be employed as PCs for driving organic transformations.

Chapter 2 discusses the employment of the beforementioned Fe-NHC complexes as PCs in the atom transfer radical addition (ATRA) reaction. After a preliminary investigation into the compatibility of the redox potentials of the complexes **7**, **8** and **9** with the ATRA substrates, it was hypothesised that Fe-NHC complexes could function as PCs to drive the ATRA reaction forward. Various photoreactor setups were tested and reaction optimisations were performed. Subsequently, the substrate scope was established, a mechanism was proposed for both the reductive and oxidative quenching routes, and the successful application of **7** and **8** as Fe-NHC PCs in the ATRA reaction was shown.

Chapter 3 describes the investigation of the performance of Fe-NHC complexes **7**, **8** and **9** as PCs in the base-promoted homolytic aromatic substitution (BHAS)

reaction. A preliminary assessment of the feasibility of combining Fe-NHC complexes **7**, **8** and **9** with BHAS substrates was conducted. This led to the hypothesis that BHAS reactions could be successfully driven by Fe-NHC PCs. Initial experimental investigations showed that PC **9** was able to catalyse the BHAS reaction, upon which further reaction optimisations, isolation of products and mechanistic investigations were conducted.

2 Atom transfer radical addition (ATRA) reactions (Paper I)

2.1 Background

Since its invention by Kharasch in the 1940s,[30–32] the atom transfer radical addition (ATRA) reaction has been established as a facile method for the functionalisation of alkenes or alkynes. In this reaction, typically a C–X (X = halogen atom) σ-bond is broken and added over the π-bond of an alkene (or alkyne), generating two new σ-bonds. Traditional methods for performing ATRA reactions involve the use of harsh radical initiators in stoichiometric amounts,[30–34] or the employment of TM-catalysts as halogen atom transfer (XAT) agents.[35–38] However, the latter catalytic procedures generally still require high temperatures or the use of toxic reagents to proceed. One example of the synthetic applicability of the ATRA reaction is the synthesis of organic molecules featuring a fluorinated motif, also known as fluorous tagging. This strategy has been useful in the facilitation of the isolation of such fluorinated products by solid-phase extraction (SPE).[39]

In Scheme 3, a general schematic overview of the ATRA reaction is provided. Upon the initiation step (traditionally a radical initiator is required here), an alkyl radical (**11**) and a halide anion (**12**) are generated from the alkyl halide starting material (**10**). This alkyl radical (**11**) then adds to the double bond of the alkene (**13**) (or alkyne), resulting in the formation of another alkyl radical (**14**). Subsequently, this reactive intermediate (**14**) can abstract a halide radical from the alkyl halide starting material (**10**), leading to the formation of the ATRA product (**15**). The alkyl radical (**11**) generated in the product-forming step can be used in a radical chain propagation mechanism.

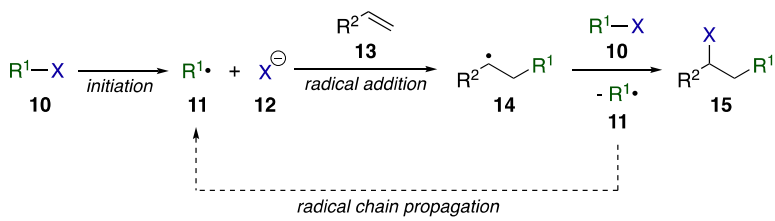

Scheme 3. Schematic overview of the general pathway for ATRA reactions. Adapted from ref. 40.

As mentioned before, there has been a surge in reports on organic transformations being driven by photoredox catalysis. The ATRA reaction has become one of the benchmark reactions for probing the functionality of novel PCs. For example, there are various reports on ATRA reactions being successfully driven by ruthenium-, iridium- or copper-based PCs and visible light.[40–42]

Fe-NHC PCs **7**, **8** and **9** absorb in the green region of the visible light spectrum. Hence, these complexes have the benefit of being excited by light of lower energy than the conventional blue light-absorbing ruthenium or iridium polypyridyl complexes, in addition to the advantage of being based on an Earth-abundant metal. Therefore, we were interested in exploring the utilisation of Fe-NHC PCs **7**, **8** and **9** to drive the ATRA reaction under green light irradiation.

2.2 Reaction optimisations and photoreactor setups

2.2.1 Reaction setup A

Iridium PC **16** ($[Ir\{dF(CF_3)ppy\}_2(dtbbpy)]^+$,[43] Figure 6) has been previously employed in the benchmark ATRA reaction illustrated in Scheme 4.[42] This complex exhibits ES redox potentials of $E°(Ir(IV)/^*Ir(III)) = –1.27$ V and $E°(^*Ir(III)/Ir(II)) = 0.83$ V vs $Fc^{+/0}$ (reported as $E°(Ir(IV)/^*Ir(III)) = –0.89$ V and $E°(^*Ir(III)/(II)) = 1.21$ V vs SCE), with an ES lifetime of 2.3 μs.[43–45] Upon excitation, Ir-PC **16** is able to reduce the substrate, diethyl bromomalonate (**18**) (reduction potential of –1.0 V vs $Fc^{+/0}$, reported as –0.62 V vs SCE)[45,46], in presence of 2 equiv of LiBr as a Lewis acid activating agent. In this reaction, the substrate is added over the 5-hexen-1-ol (**17**) double bond (0.5 mmol scale), in presence of 1 mol% of PC **16** under 24 h of irradiation with blue light (λ = 435 nm) under inert conditions.[42]

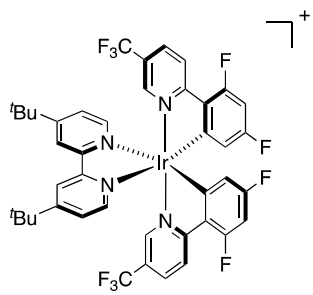

16

τ_0 = 2.3 μs (^{3}MLCT)

Figure 6. The chemical structure and ES lifetime of $[Ir\{dF(CF_3)ppy\}_2(dtbbpy)]PF_6$ (**16**).[42,43]

These reaction conditions were used as a starting point to investigate the photoredox catalytic abilities of iron complex **9**, which was chosen due to its prolonged ES lifetime (τ_0 = 2 ns, ^{2}LMCT) and beneficial ES redox potentials ($E°$(Fe(IV)/*Fe(III)) = –1.88 V and $E°$(*Fe(III)/Fe(II)) = 1.0 V vs $Fc^{+/0}$).[10]

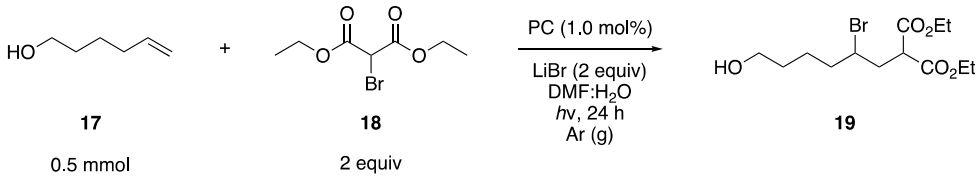

17 0.5 mmol **18** 2 equiv **19**

Scheme 4. A benchmark ATRA reaction using 1.0 mol% PC on 0.5 mmol scale.

The irradiation wavelength for this experiment was chosen according to the absorption spectrum of PC **9** (Figure 7), which exhibits an absorption maximum at λ = 502 nm.[10] The first attempt to perform photoredox catalysis using **9** as PC was hence done under λ = 545 nm LED irradiation (green, 3.2 mW/LED output power) for 24 h in a 10 mL Schlenk tube under argon atmosphere and continuous stirring (Figure 8, setup **A**). This did not lead to any conversion of starting material, as assessed by both TLC (thin-layer chromatography) and ^{1}H NMR analysis.

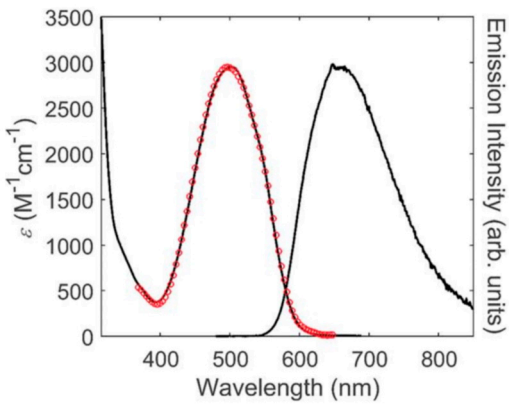

Figure 7. Absorption (left, red) and emission spectrum (right, black) of PC **9**. Adapted from ref. 10.

The same procedure was attempted using Fe-PC **9** under blue LED irradiation (λ = 450 nm, 24 mW/LED output power) instead, as this would provide photons of higher energy as well as a higher photon flux. PC **9** also exhibits decent absorption at that wavelength, therefore making it compatible with irradiation with blue light. This change of the light source resulted in trace amounts (approx. 4%) of product being observed when analysing the reaction crude by ^{1}H NMR.

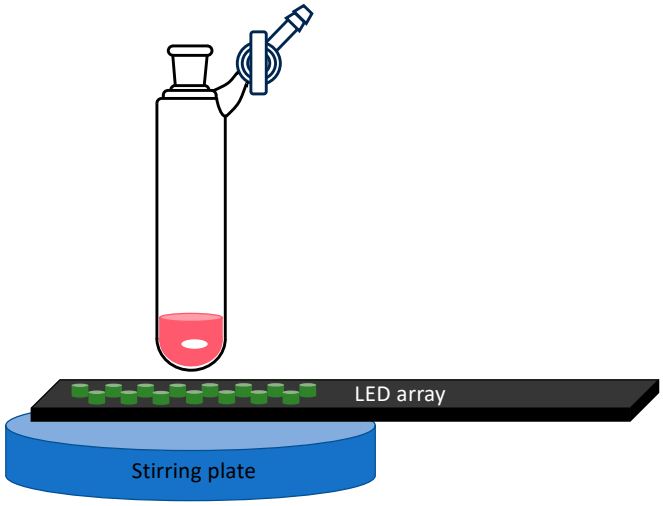

Figure 8. Schematic overview of photoredox catalysis setup **A.**

2.2.2 Reaction setup B

Since only minor conversion was observed for the previously studied ATRA reaction using PC **9**, the setup was altered in an attempt to increase the reaction performance. In this new setup (Figure 9), designed by Jens Uhlig (Chemical Physics, Lund University), an aluminium block with eight cylindrical holes was used, which fit eight 4 mL screw-cap vials in parallel. This setup allowed for approximately three LEDs to irradiate each individual vial from the bottom, also reflecting the LED light on the walls of the slots to the vial, thereby maximising the irradiation. Water cooling was enabled by channels running through the aluminium block. Furthermore, this aluminium holder was designed to fit the LED arrays that were used in setup **A**.

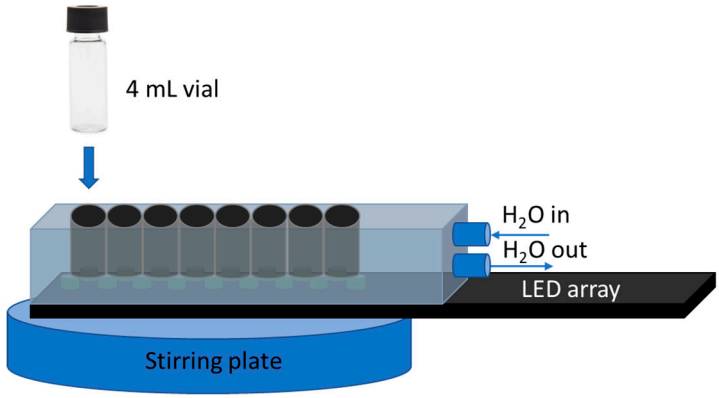

Figure 9. Schematic overview of photoredox catalysis setup **B**.

At the same time, the reaction itself was adapted to involve a more reactive substrate, taking advantage of C–I bonds being relatively more easily reduced than C–Br bonds.[41] In this ATRA reaction (Scheme 5), 5-hexen-1-ol (**17**) was combined with perfluoroalkyl iodide **20** or **21** with 1 mol% of PC **9** (traditionally with $[Ru(II)(bpy)_3]^{2+}$ (**2**) as PC), and sodium *L*-ascorbate (SA) (2 equiv) as a sacrificial electron donor (SED) (reduction potential of 0.1 V vs $Fc^{+/0}$)[47]. The presence of SA should drive the reaction to proceed via a reductive quenching pathway.

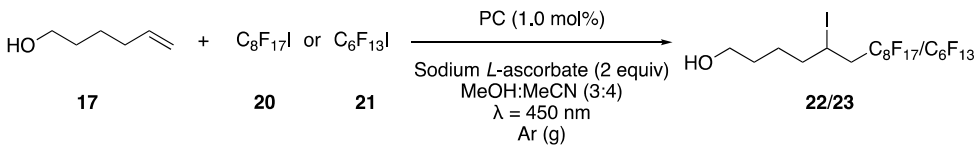

Scheme 5. The ATRA reaction utilising perfluoroalkyl halides.[41]

A screening of four parallel reactions in reaction setup **B** (two vials with substrate **20** and two vials with substrate **21**) showed minor conversion on TLC after 24 h of irradiation (Table 1, entry 1 and 3). The reaction mixtures were tracked by TLC until full conversion was observed after six days (entry 2 and 4). After pooling of the two duplicate reaction mixtures for each product, a standard workup was performed. The mixtures were purified by silica column chromatography (1 x 10 cm, 4:1 hexane–ethyl acetate (EtOAc)), providing pure **22** (0.085 g, 0.13 mmol, 53%) and **23** (0.079 g, 0.14 mmol, 58%). Repeating the reaction, workup and purification for substrate **20**, provided product **22** in an improved yield (0.062 g, 0.10 mmol, 77%). These results show that photoredox catalysis could be driven using PC **9**. However, further improvements could be made to both the purification procedure as well as the reaction itself.

Table 1. Overview of the results using setup **B**. All reactions were performed in presence of substrate **17** (0.125 mmol) and 1.0 mol% PC **9** under λ = 450 nm irradiation and argon atmosphere.

Entry	Substrate	SA	Reaction time	Conversion (TLC)	Isolated yield (%)
1	$C_8F_{17}I$ (**20**)	2 equiv	24 h	Minor	-
2			6 days	Full	53
3	$C_6F_{13}I$ (**21**)	2 equiv	24 h	Minor	-
4			6 days	Full	58–77

2.2.3 Reaction setup C

The irradiation intensity of each individual reaction slot in reaction setup **B** was measured with an illuminometer (measured on top of each slot). This showed large variation from 0.036 W/slot to 0.059 W/slot, most likely due to a misalignment of the LEDs under the reaction slots. For this reason, the commercially available EvoluChem PhotoRedOx Box™ (Hepatochem) (Figure 10) was purchased.[48] In this photoreactor, the light originates from a more powerful light source (38 W, λ = 450 nm, 0.45 W effective power), and is directed by mirrors towards the samples in the sample holder. It was hypothesised that the use of such a setup would lead to a more intense and equal irradiation of the reaction mixtures. Another benefit of setup **C** is that it allows for different types of reaction vessels, for example Schlenk tubes, 4 mL vials and NMR tubes.

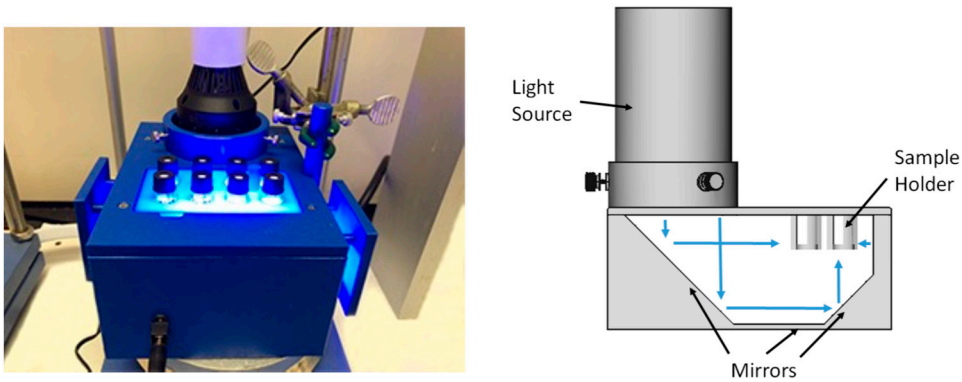

Figure 10. Picture and schematic overview of photoredox catalysis setup **C**: The EvoluChem PhotoRedOx Box™.[48]

Employing reaction setup **C** with two 10 mL Schlenk tubes (0.25 mmol **17**, 2 equiv **20** or **21** and 2 equiv SA), one for each perfluoroalkyl halide substrate, only minor

conversion to products **22** and **23** was observed after one week of tracking by TLC (Table 2, entry 1 and 2). The worse reactivity could be due to the relatively larger reaction volume in setup **C** compared to setup **B**, meaning that the exposed surface and the effective irradiation per volume is less than if the mixture would have been divided into smaller batches.

Therefore, the scale of the reaction was lowered to 0.125 mmol of **17** (half scale) in 4 mL vials. Furthermore, a follow-up study on the photocatalysed ATRA reaction showed improved results when utilising 1.33 equiv of **20** and 0.35 equiv of SA instead.[41] Employment of these altered reaction conditions in setup **C** gave 97–99% ^{1}H NMR yield of product **22** after 18 h of irradiation (entry 3) and 94% ^{1}H NMR yield after 10 h of irradiation (entry 4). These yields were determined by ^{1}H NMR analysis of aliquots of the reaction mixture which were diluted in deuterated methanol (CD_3OD) with toluene as an IS.

Table 2. Overview of the results using setup **C**. All reactions were performed in presence of 1.0 mol% PC **9** under λ = 450 nm irradiation and argon atmosphere.

Entry	**17**	Substrate	SA	Reaction time	Result
1	0.250 mmol	$C_8F_{17}I$ (**20**) (2 equiv)	2 equiv	1 week	TLC showed minor conversion
2		$C_6F_{13}I$ (**21**) (2 equiv)			
3	0.125 mmol	$C_8F_{17}I$ (**20**) (1.33 equiv)	0.35 equiv	18 h	97–99% ^{1}H NMR yield
4				10 h	94% ^{1}H NMR yield

Control reactions were performed in setup **C** (Table 3). The optimal reaction conditions obtained in Table 2 are also provided in Table 3 (entry 1). Using $[Fe(bpy)_3](PF_6)_2$ as PC instead of PC **9**, showed minor conversion to product **22** on TLC after two days of irradiation (entry 2). ^{1}H NMR analysis indicated decomposition of the complex, which most likely hampered the reaction since prolonged irradiation did not improve the conversion. Using $FeBr_3$ gave approx. 40% ^{1}H NMR conversion after two days of irradiation (entry 3). This was not entirely unexpected, since $FeBr_3$ is known to catalyse a reaction akin to the ATRA reaction: the Atom Transfer Radical Polymerisation (ATRP) reaction.[49] In the ATRP reaction, $FeBr_3$ is used as a XAT agent to 'shuttle' Br atoms between substrates and products under irradiation.

Table 3. Overview of control reactions in setup **C** using various PCs and varying conditions. 0.125 mmol of **17**, 1.33 equiv of **20**, 0.35 equiv of SA, 1 mol% of PC.

Entry	PC	Irradiation wavelength (λ)	Atmosphere	Reaction time	Result
1	**9**	450 nm	Argon	10 h	94% ^{1}H NMR yield
2	$Fe(bpy)_3(PF_6)_2$	450 nm	Argon	2 days	TLC showed minor conv.
3	$FeBr_3$	450 nm	Argon	2 days	40% ^{1}H NMR conversion
4	**9**	450 nm	Air	4 days	No product formation
5	**9**	-	Argon	5 days	No product formation
6	-	450 nm	Argon	5 days	TLC showed minor conv.
7	-	-	Argon	5 days	No product formation

Repeating the experiment in air or in the dark with PC **9** did not yield any observable product formation (entry 4 and 5). Without any PC, minor conversion was observed by TLC after 5 days of irradiation (entry 6), whilst not showing any conversion in the dark (entry 7). These findings indicate that the reaction in presence of PC **9**, at these irradiation intensities, outperforms the observed background reaction. Furthermore, these results show that an argon atmosphere and irradiation are necessary for the reaction to proceed.

To probe if oxidative quenching can occur using PC **9**, the reaction was repeated without sacrificial electron donor (i.e. SA) using the optimised conditions for the reductive quenching route in a 4 mL vial (0.125 mmol **17**, 1.33 equiv **20**, 1 mol% PC, 0.75 mL CD_3OD, 1.00 mL CD_3CN (deuterated acetonitrile)), which led to a plateau at 91% conversion (determined by ^{1}H NMR) after 20 h of irradiation. This showed that oxidative quenching in fact could occur using PC **9**, but that further optimisations were needed.

2.2.4 Reaction setup D

To investigate if an even higher irradiation intensity would improve the reaction times further (compare: 0.036–0.059 W in setup **B** and 0.45 W in setup **C**) a TAK120 photoreactor (HK Testsysteme GmbH, Figure 11, setup **D**) was purchased, which provides 6.73 W/slot irradiation at λ = 455 nm. The slots inside of this photoreactor allow for the use of ten 6–10 mL reaction vials in parallel. The reactor is air-cooled and tracks the sample temperature via a temperature probe.

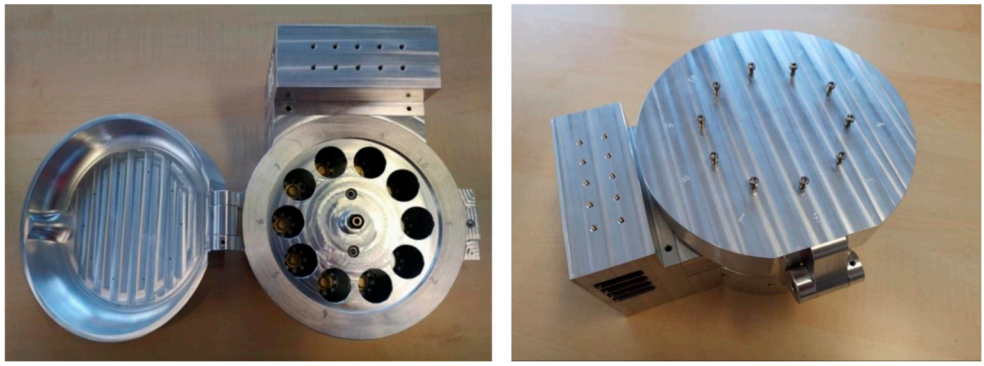

Figure 11. Pictures of photoredox catalysis setup **D**: The TAK120 photoreactor (HK Testsysteme GmbH).[50]

An initial run with the previously optimised conditions at double the scale (0.25 mmol **17**, 1.33 equiv **20**, 0.35 equiv SA, 1 mol% PC **9**, 1.5 mL CD_3OD, 2.0 mL CD_3CN, argon atmosphere) in a 10 mL screw-cap vial under $\lambda = 455$ nm irradiation indicated full conversion to **22** by ^{1}H NMR analysis after 18 h of irradiation (Table 4, entry 1). To probe the reaction time, the reaction was repeated, showing full conversion by ^{1}H NMR after just 4 h (entry 2). Shortening the reaction time even further to 2 h, provided 97% conversion by ^{1}H NMR (entry 3).

Table 4. Overview of the initial results of the ATRA reaction in setup **D**. Reaction conditions: 0.25 mmol of **17**, 1.33 equiv of **20**, 1 mol% PC **9**, 3.5 mL solvent, under $\lambda = 455$ nm irradiation and argon atmosphere.

Entry	Reaction time	Cycle	Solvent system	^{1}H NMR yield
1	16 h	Reductive	CD_3OD–CD_3CN (1.5:2.0 mL)	>99%
2	4 h	Reductive		>99%
3	2 h	Reductive		97%
4	22 h	Oxidative		28%
5	22 h	Oxidative	DMSO-d_6 (3.5 mL)	44%

The oxidative ATRA reaction was tested under the same reaction conditions (0.25 mmol **17**, 1.33 equiv **20**, 1 mol% PC **9**) in either the CD_3OD–CD_3CN (1.5:2.0 mL) solvent mixture, or 3.5 mL of deuterated dimethyl sulfoxide (DMSO-d_6).[41] After 22 h of irradiation, 28% conversion was observed for the CD_3OD–CD_3CN reaction mixture (entry 4), whereas 42% conversion was observed in DMSO-d_6 (entry 5), indicating that the latter solvent led to superior results for the oxidative ATRA reaction.

However, it is worth noting the difference between the results obtained in setup **C** and setup **D**. In setup **C**, the oxidative ATRA reaction (although in half the reaction mixture size) reached 91% conversion after 20 h. The most likely reason for this was that the reaction temperature went up towards 50 °C after prolonged irradiation periods in setup **D**. This in turn led to the evaporation of solvent, as well as apparent degradation of the reaction system (a brown–orange sludge was obtained in contrast to the reddish solution observed in the previous setup). The photoreactor supplier confirmed that the reactor was in fact malfunctioning, probably due to an extensive vial diameter, hampering air cooling, thus degrading the LED array much faster than anticipated.

The photoreactor unit was replaced and the vial size was changed to a 6 mL crimp vial. The performance of this new unit was confirmed by rerunning the reductive ATRA reaction, which indicated 98% conversion after 2 h of irradiation and full conversion after 3 h.

Having established the optimised reaction conditions for the reductive ATRA reaction in setup **D**, control experiments were performed (Table 5). Surprisingly, it was discovered that a considerable background reaction was taking place under the previously established reductive reaction conditions (λ = 455 nm irradiation, varying intensities, entry 1–4). Without irradiation, in presence of PC **9**, no conversion was observed (entry 5).

Table 5. Overview of the control experiments in reaction setup **D**. Reaction conditions: 0.125 mmol of **17**, 1.33 equiv of **20**, 0.34 equiv SA, 0.75 mL CD_3OD, 1.00 mL CD_3CN under argon atmosphere.

Entry	Irradiation wavelength (λ)	Intensity (W/slot)	PC loading	Reaction time	^{1}H NMR yield
1	455 nm (blue)	7.03	-	2 h	>99%
2	455 nm (blue)	5.04	-	2 h	97%
3	455 nm (blue)	3.45	-	12 h	>99%
4	455 nm (blue)	0.82	-	20 h	0–46%
5	-	-	1% PC **9**	21 h	No conversion
6	530 nm (green)	3.03	-	60 h	No conversion
7	530 nm (green)	3.03	1% PC **9**	17 h	83–99%

The irradiation wavelength was therefore altered to λ = 530 nm irradiation (green light, 3.03 W/vial), because PC **9** exhibits high absorption at that wavelength, while the lower energy light might not provide enough energy to drive the background reaction. This was confirmed as no background reaction was observed in absence of

PC **9** under green light irradiation (entry 6). In presence of 1 mol% of PC **9**, 83–99% conversion was obtained after 17 h of irradiation with green light (entry 7).

Stern–Volmer quenching studies of PC **9** with different SEDs indicated that triethylamine (TEA) would be a suitable alternative to SA, which also possesses a fitting oxidation potential (0.31 V vs $Fc^{+/0}$, reported as 0.69 V vs SCE)[45,51] as well as superior solubility in the solvent system. Repeating the reaction using 1 equiv of TEA as SED under the standardised conditions (λ = 530 nm irradiation) reduced the reaction time to 2 h (87–94% ^{1}H NMR yield).

For the oxidative ATRA reaction (λ = 530 nm irradiation), it was observed that DMSO-d_6 gave superior results (61–66% yield after 12 h of irradiation) compared to the CD_3CN–CD_3OD solvent mixture (no conversion after 25 h of irradiation).

2.3 Optimised conditions and substrate scope

With a functional method for the reductive and oxidative ATRA reaction established, the performance of PC **9** was compared to Fe-NHC PC **8** ($[Fe(btz)_3](PF_6)_3$). It was observed that the exchange of PC **9** for PC **8** reduced the reaction time from 2 h to 10 min for the reductive ATRA reaction and from a moderate 61–66% yield in 12 h to full conversion in 40 min for the oxidative ATRA reaction. This increase in reactivity could be due to the poor cage escape yields associated with the use of PC **9**, especially in solvents such as acetonitrile and with TEA as SED.[52–54]

Thorough reaction optimisations were performed for both the reductive and oxidative ATRA reactions (for the addition of **20** to **17**), establishing the optimal conditions as provided in Scheme 6. Various SEDs were investigated, but a substoichiometric amount of 0.34 equiv of TEA was found to be ideal to drive the reductive ATRA reaction forward. Additionally, catalyst loadings of 0.5 mol% and 1.5 mol% of PC **8** were established for the reductive and oxidative routes, respectively. Optimal reactivity and solubility of the reactants was observed using methanol–acetonitrile (3:4) as a solvent mixture for the reductive ATRA reaction, whereas acetonitrile was the ideal solvent for the oxidative reaction.

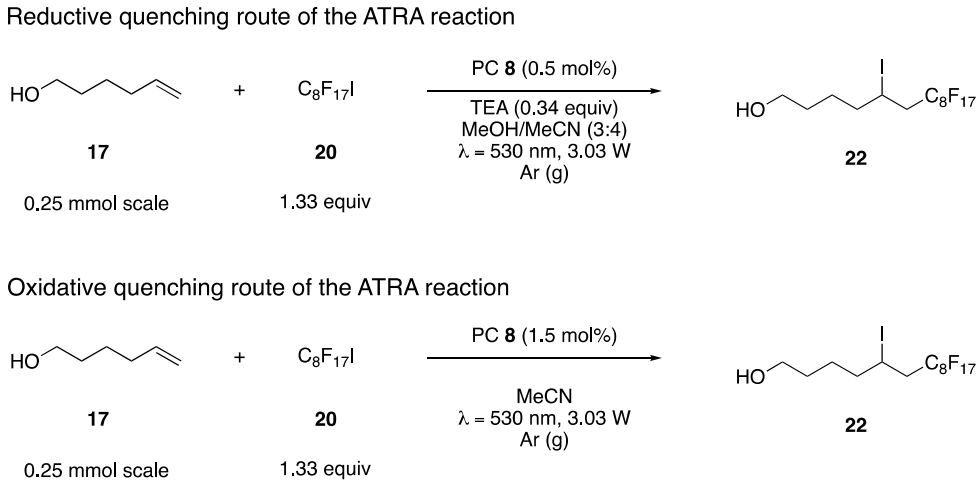

Scheme 6. Optimised reaction conditions for the reductive and oxidative quenching routes of the ATRA reaction.

2.3.1 Reductive quenching route

Various perfluoroalkyl halides and $CBrCl_3$ (entry 3) were added to the substrates (Table 6), employing the previously established optimised reaction conditions (Scheme 6). Moderate to high yields were observed for the addition to terminal alkenes and an alkyne (entry 1–6 and 9–12). Among these, slightly lower yields were obtained for the nitrile-containing substrate **27** (entry 5), which could be attributed to the quenching of PC $\mathbf{7}^*$ by the low-lying LUMO of the nitrile group (PC **7** is the Fe(II) analogue of Fe(III)-NHC **8**; the involvement of PC **7** in the catalytic cycle will be discussed in the mechanistic investigations section of this chapter). Diminished reactivity was observed for cyclohexene (entry 7), likely because of its less sterically accessible alkene moiety. However, norbornene (entry 8), which also contains an internal alkene, showed higher reactivity, which is most likely due to its ring strain. Under these reaction conditions, the alkyne substrate **35** also exhibited good reactivity (entry 9), although prolonged irradiation times were necessary. The presence of a carbonyl functional group did not negatively influence the reactivity (entry 11 and 12). However, for the substrate containing a carboxylic acid, a mixture of the desired product **40** and a lactone side-product **41** was observed (entry 11). The lactonization of **40** to **41** is presumably induced by the presence of the TEA base in the reductive quenching reaction conditions. Although the expected preference for external over internal alkenes was confirmed by substrate **44** (entry 13), a diminished yield was observed, due to the terminal alkene being relatively sterically hindered. Probing the preference for alkyne moieties over alkenes, showed a preference for the latter (entry 15), which is in line with the observed reduced

reactivity for alkyne-containing substrate **35**. This substrate also illustrates the presence of radicals in this reaction, as ring-closed products are generated (**49-*E*** and **49-*Z***). Although diethyl bromomalonate (**18**) did not exhibit the desired reactivity in this reaction system, moderate yields were observed for the intramolecular reaction of a substrate containing the bromomalonate moiety (entry 14). An additional limitation is the addition of the perfluoroalkyl iodide to Michael acceptors, in which no product formation was observed.

A variety of control experiments was conducted. The employment of alternative Fe-based PCs, such as $FeBr_2$, $FeBr_3$ and $[Fe(bpy)_3]^{2+}$ did not lead to notable conversion of the substrates. Experiments in absence of irradiation or PC did not lead to any conversion, confirming the necessity for PC **8** and light for the reaction to proceed. For $[Ru(bpy)_3]^{2+}$ (PC **2**), full conversion was observed when irradiating with higher energy blue light (λ = 455 nm, 6.18W) for 4 min, which is shorter than the necessary 8 min for PC **8** (green light, λ = 530 nm, 3.03 W).

2.3.2 Oxidative quenching route

The optimised reaction conditions for the oxidative quenching route (Scheme 6) were applied to the same range of substrates. Similar results were obtained for many of the substrates, although slightly longer reaction times were generally necessary. The reaction employing substrate **27** (entry 5) exhibited slightly worse reactivity, however, substrates **29** and **35** (entry 6 and 9) were more reactive under the oxidative reaction conditions. As expected, no lactone product **41** was formed under these conditions (i.e. in absence of TEA). Under these conditions, Michael acceptors were unreactive as well.

The same control experiments were conducted as previously discussed for the reductive quenching route. The other Fe-based PCs ($FeBr_2$, $FeBr_3$ and $[Fe(bpy)_3]^{2+}$) did not catalyse the reaction under the oxidative ATRA conditions. Without irradiation or in absence of PC, no conversion was observed. Probing the oxidative reaction conditions with $[Ru(bpy)_3]^{2+}$ (PC **2**) instead of the Fe-PC, indicated that 34% conversion was reached after 40 min, which is significantly worse than the >99% conversion that was obtained with PC **8** after the same irradiation time. This could be due to PC **2** exhibiting poor absorption of green light.

Although the oxidative quenching route proceeds in absence of a SED, higher catalyst loadings and longer reaction times were generally necessary. Furthermore, the longevity of PC **8** was better in the reductive than in the oxidative route. An experiment in which repeatedly fresh starting materials were added to the reaction mixture once full conversion was reached, before continuing irradiation, showed that PC **8** continued to be active under several of such cycles under reductive quenching conditions.

Table 6. Scope of the ATRA reaction through reductive (RQ) and oxidative (OQ) quenching of PC **8**. Reaction conditions: RQ: 0.5 mol% PC (**8**), TEA (0.34 equiv), R–X (1.33 equiv), 4:3 MeCN–MeOH. OQ: 1.5 mol% PC (**8**), R–X (1.33 equiv), MeCN. Adapted from Paper I. (Table continues on next page)

Entry	Substrate	Route	Time (min)	Product	Isolated yield (%)
1	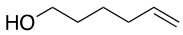 **17**	RQ	10	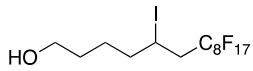 **22**	91
		OQ	40		92
2		RQ	10	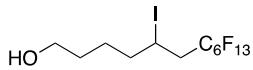 **23**	93
		OQ	40		93
3		RQ	60	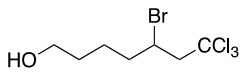 **24**	43
		OQ	40		35
4	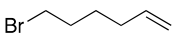 **25**	RQ	10	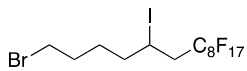 **26**	90
		OQ	40		94
5	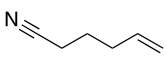 **27**	RQ	40	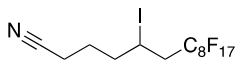 **28**	76
		OQ	40		57
6	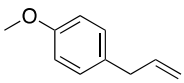 **29**	RQ	40	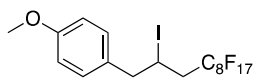 **30**	58
		OQ	80		74
7	 **31**	RQ	15	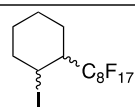 **32-*cis*, 32-*trans***	22 (*cis*–*trans* 17:5)
		OQ	40		32 (*cis*–*trans* 25:7)
8	 **33**	RQ	15	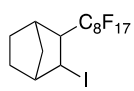 **34**	80
		OQ	40		91

Table 6. (Continued) [a]Intramolecular reaction in absence of external halide source.

Entry	Substrate	Route	Time (min)	Product	Isolated yield (%)
9	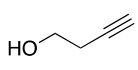 **35**	RQ	20	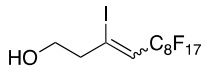 **36-*E*, 36-*Z***	62 (*E*–*Z* 42:20)
		OQ	80		92 (*E*–*Z* 65:15)
10	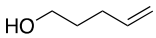 **37**	RQ	10	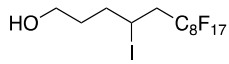 **38**	93
		OQ	40		89
11	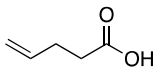 **39**	RQ	30	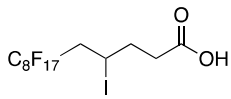 **40**	43
		OQ	40		87
		RQ	30	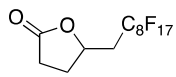 **41**	26
12	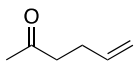 **42**	RQ	15	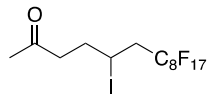 **43**	98
		OQ	40		97
13	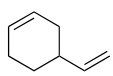 **44**	RQ	30	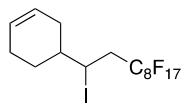 **45**	63
14[a]	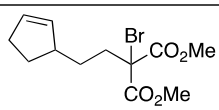 **46**	RQ	45	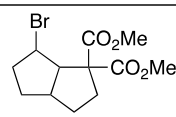 **47**	49
		OQ	40		31
15	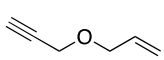 **48**	RQ	150	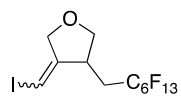 **49-*E*, 49-*Z***	51 (*E*–*Z* 25:26)
		OQ	150		49 (*E*–*Z* 25:24)

2.4 Mechanistic investigations

2.4.1 Reductive quenching route

In the reductive quenching cycle (Scheme 7), firstly, PC **8** is excited to the ^{2}LMCT state (**8***), after which reductive quenching by TEA converts it to the Fe(II)-NHC PC **7**. A rather unique second excitation of PC **7** to a ^{3}MLCT state (**7***) generates a much stronger reductant (–1.6 V vs $Fc^{+/0}$)[28], which allows oxidative quenching to take place by substrate **20**. This regenerates PC **8** and initiates a radical chain mechanism, which upon the addition to alkene **17** leads to the formation of product **22**. Here, two photo-induced electron transfer processes take place consecutively (conPET), giving access to an additional, higher energy ^{3}MLCT state. Although reports on such 'Z-schemes' can be found in the field of artificial photosynthesis,[55] this is a rather unique mode of action for photoredox catalysis using TM-complex PCs.[56]

The proposed mechanism is supported by a variety of experiments. The presence of radical intermediates was corroborated by the addition of TEMPO to the reaction mixture, which completely hampered the reaction. As mentioned previously, the intramolecular reaction on substrate **48** (entry 15), the ring-closing reaction on diethyl 2,2-diallylmalonate and ring-opening reaction of *trans*-(2-vinylcyclopropyl) methanol also are indicative of the presence of radical intermediates in this reaction.

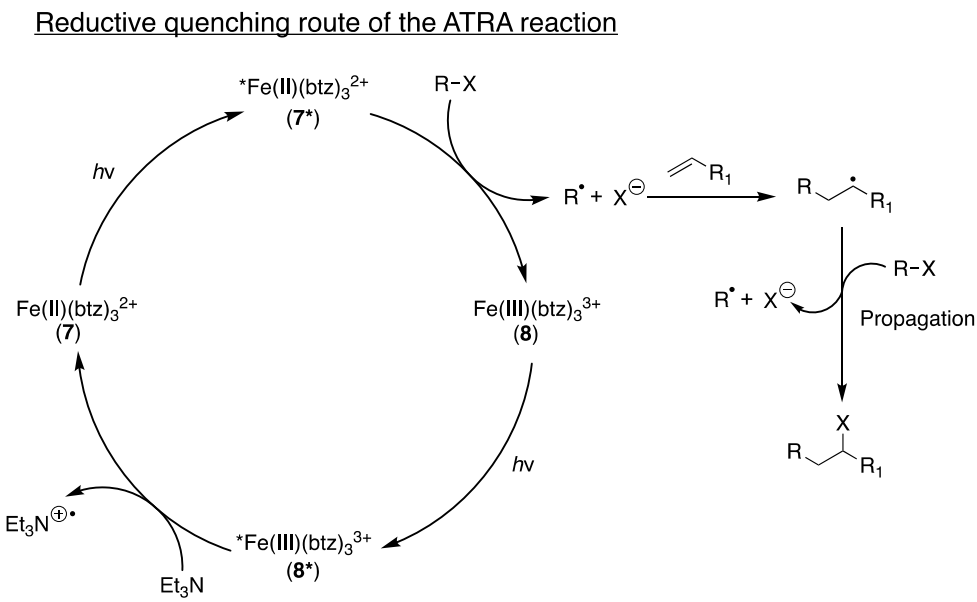

Scheme 7. Proposed catalytic scheme for the reductive quenching mechanism of the ATRA reaction. Adapted from Paper I.

An irradiated mixture containing PC **8** and TEA was analysed by UV-Vis absorption spectroscopy, which showed the presence of PC **7**. This is in line with the proposed mechanism, where the ^{2}LMCT state of **8*** is reductively quenched by TEA to generate the Fe(II)-species **7**. Stern–Volmer quenching studies showed that this rather short-lived ES is quenched with an efficiency of $\eta_q = 31\%$, with a diffusion controlled bimolecular rate constant k_q of $8.4 \cdot 10^9$ M^{-1} s^{-1}. Transient absorption (TA) spectroscopy showed that the production of **7** by the reductive quenching of **8*** proceeds with a quantum yield of $\eta_q\eta_{ce} = 9\%$. The rather low quenching efficiency is compensated by a substantial cage escape yield of $\eta_{ce} > 20\%$, which is significantly larger than the poor cage escape yields generally found for PC **9*** (for example, $\eta_{ce} = 2\%$ in acetonitrile with *N*,*N*-dimethylaniline (DMA) as quencher.[52–54] This could be the reason for why PC **8** (and indirectly PC **7**, the Fe(II)-analogue of PC **8**) outperforms PC **9** in this reaction.

In the next step of the proposed mechanism, PC **7** is excited to **7*** (^{3}MLCT), before reducing the $C_8F_{17}I$ substrate (**20**). A sample containing **7** and $C_8F_{17}I$ (**20**) was exposed to ambient light, after which analysis by UV-Vis absorption spectroscopy indicated the regeneration of PC **8**. In absence of light, no such conversion was observed. This implies that the strongly reducing PC **7*** (–1.6 V vs $Fc^{+/0}$)[28] exhibits a sufficiently long ES lifetime (330 ps in MeCN–MeOH (4:3)) to allow for the oxidative quenching by the perfluoroalkyl iodide substrate (**20**).

To further support this double excitation mechanism, a wavelength switching experiment was designed (Figure 12). Two parallel vials containing PC **8**, substrate **17** and TEA (Figure 12, UV-Vis absorption spectrum, red line) were irradiated by green light ($\lambda = 525$ nm), which led to the in situ generation of PC **7** (Figure 12, UV-Vis absorption spectrum, brown line). After addition of **20**, and keeping the reaction mixture in the dark, no product formation was observed (Figure 12, vial C). This led to the conclusion that PC **7** itself cannot reduce the substrate. The duplicate was then irradiated at $\lambda = 700$ nm, exclusively generating PC **7***, which allows the catalytic cycle to close upon quenching by **20**. This irradiation wavelength was chosen due to the lack of absorption of PC **8** at that wavelength. Analysis of the resulting mixture by UV-Vis spectroscopy showed the regeneration of PC **8**, and a product formation of 5%. As only 0.5% of PC **8** was present in the reaction mixture, this implies that it is likely that a radical propagation mechanism is present. This is further supported by the fact that a substoichiometric amount of SED is necessary to drive the reaction to completion.

TA spectroscopy showed the regeneration of PC **8** from PC **7** upon laser flash excitation ($\lambda = 650$ nm), in presence of the perfluoroalkyl halide (**20**). The oxidative quenching of **7*** by **20** was determined to proceed with a quantum yield of $\eta_q\eta_{ce} = 18\%$. This step (the formation of **8**) is also necessary for the catalytic cycle to close.

The next step in the mechanism is the alkene or alkyne being attacked by the alkyl radical, which generates an alkyl- or alkenyl-radical, respectively. The product formation from these reactive radical intermediates could involve a radical chain mechanism. Chemical actinometry experiments[57,58] can be employed to determine photon fluxes and quantum yields (Φ) for photochemical reactions. If the obtained Φ exceeds 1, this supports the presence of a radical chain mechanism. A quantum yield of Φ = 6 was obtained (after correcting for the necessity for two photons to effect one turnover), which implies that the presence of a radical chain pathway is probable.

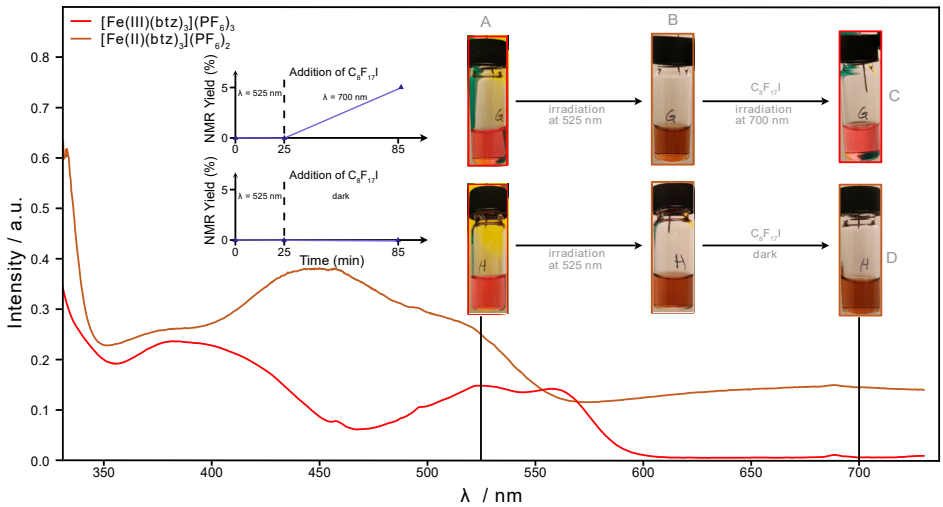

Figure 12. Overview of the wavelength-switching experiment for the ATRA reaction, employing PC **8**, 5-hexen-1-ol (**17**) and perfluorooctyl iodide (**20**). Reprinted from Paper I.

2.4.2 Oxidative quenching route

In the oxidative quenching cycle (Scheme 8), PC **8** is excited to **8*** (^{2}LMCT, τ_0 = 100 ps in acetonitrile[27]), which is oxidatively quenched by substrate **20**. This generates the oxidised Fe(IV)-NHC PC **7'**, which then via SET from a radical alkyl intermediate returns to PC **8**.

Radical trapping experiments were performed for the oxidative quenching route as well and no product formation was observed upon addition of TEMPO. Furthermore, the intramolecular reaction with substrate **48** (Table 6, entry 15), the ring-closing reaction with diethyl 2,2-diallylmalonate and the ring-opening reaction of *trans*-(2-vinylcyclopropyl) methanol proceeded in agreement with the presence of radical intermediates in this reaction mechanism.

In this case, no TEA, and hence no **7***, is available to induce the reductive cleavage of the perfluoroalkyl halide substrate. Therefore, it is most likely that PC **8*** is oxidatively quenched by the substrate, generating the oxidised Fe(IV)-PC **7'**. However, it could not be excluded that ligand oxidation potentially could occur instead.

In the acetonitrile–methanol (MeCN–MeOH, 4:3) solvent mixture, no emission quenching was observed of **8*** by **20**. However, in pure acetonitrile, weak quenching of the ^{2}LMCT state was experimentally observed (η_q = 9%). This is in line with acetonitrile being the optimal solvent for this reaction. In this case, because of the low quenching yield, no charge separated products could be observed by TA spectroscopy. Control experiments such as excluding irradiation and performing the reaction in absence of PC **8**, did not show any product formation.

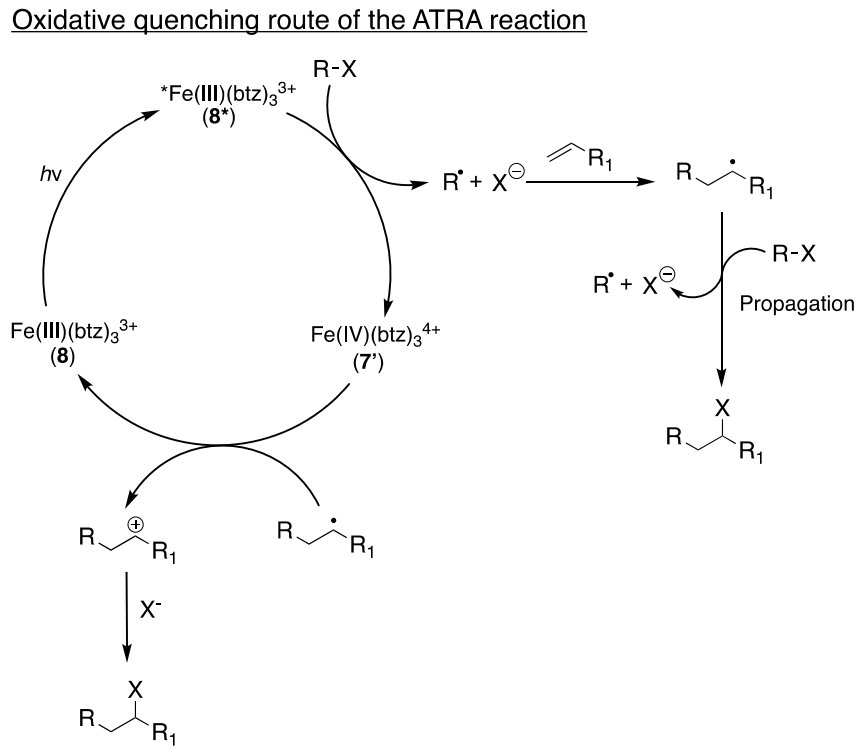

Scheme 8. Proposed catalytic scheme for the oxidative quenching mechanism of the ATRA reaction. Adapted from Paper I.

It is noteworthy that the reported reduction potential of $C_8F_{17}I$ (**20**) (–1.70 V vs $Fc^{+/0}$, reported as –1.32 vs SCE)[41,45] is more negative than the reduction potential of PC **8*** ($E°$(Fe(IV)/*Fe(III)) = –1.0 V vs $Fc^{+/0}$)[27]. Redox potentials can be used to estimate the thermodynamic driving force for electron transfer between a reductant and an

oxidant, however, a mismatch in redox potentials does not necessarily imply that the reduction of **20** by PC **8*** is impossible.[59] For example, in a previous report on a photoredox catalytic ATRA reaction, various perfluoroalkyl iodides were employed as substrates, including those with more negative reduction potentials (up to –1.5 V vs SCE) than the employed Ru-PC **2** (–1.33 V vs SCE).[41] Nonetheless, the poorly matching redox potentials probably result in the inefficient quenching of PC **8***. This, together with the rather short ES lifetime, can be contributing factors to the prolonged irradiation times necessary for reactions following the oxidative quenching cycle to reach full conversion.

Although the oxidative quenching route has the benefit of proceeding without a SED, it carries the disadvantage of generating the Fe(IV) species **7'**, which exhibits worse stability when compared to its Fe(II) counterpart (**7**).[27]

To the best of our knowledge, this is the only example where photoredox catalysis is driven by the oxidative quenching of the ^{2}LMCT state of an iron complex.

2.5 Conclusion

This chapter covered the journey towards establishing the ATRA reaction driven by Fe-NHC complexes and visible light. Initially, various photoreactor setups were probed with Fe-NHC complex **9** as PC. However, under the most powerful irradiation conditions (reaction setup **D**, blue light irradiation), it was observed that the reactivity of PC **9** could not outcompete the simultaneously present background reaction.

Interestingly, it was Fe-NHC PC **8** that, despite its sub-ns ES lifetime, could efficiently drive the ATRA reaction, both via a reductive and an oxidative quenching mechanism. In the reductive quenching cycle, a double excitation (conPET) mechanism was observed, which is a novel finding for Fe-PCs. Initially, via the reductive quenching of **8***, the reduced PC **7** was obtained in situ. Upon the second excitation, a more long-lived, stronger reducing ^{3}MLCT state (**7***) was accessed which could be oxidatively quenched by the substrate. Although the corresponding oxidative quenching cycle of PC **8** was found to be less efficient, it was still able to drive the ATRA reaction in absence of a SED. This exemplified the employment of a ^{2}LMCT state of an Fe-NHC complex being oxidatively quenched by the substrate.

The proposed reaction mechanisms for the reductive and oxidative quenching routes were supported by a variety of experiments. Furthermore, a broad substrate scope was established in which the synthetic utility of this reaction was shown.

This research demonstrates the potential for using Fe-NHC complexes **7** and **8** as efficient PCs, despite exhibiting sub-ns ES lifetimes. Besides the advantage of

utilising PCs based on the Earth-abundant iron, they absorb in the green area of the visible spectrum. This implies that these Fe-NHC PCs can drive the ATRA reaction by utilising photons of lower energy as compared to their noble metal counterparts. These findings establish PC **7** and **8** as appealing alternatives to the traditional Ru- or Ir-PCs within the field of visible light photoredox catalysis.

3 Base-promoted homolytic aromatic substitution (BHAS) reactions (Paper II)

3.1 Background

In the base-promoted homolytic aromatic substitution (BHAS) reaction, a C–C bond is formed between two aromatic moieties, either intra-[18] or intermolecularly[60]. Traditional methods to drive these types of reactions forward involve the use of harsh reaction conditions, which include high temperatures, microwave conditions, or strong bases, most commonly potassium *tert*-butoxide (^{t}BuOK).[61] In recent years, efforts have been made to utilise photoredox catalytic conditions, as these are generally more benign. By using milder reaction conditions, undesired side-reactions or decomposition of reaction components can be avoided. These investigations have resulted in BHAS reactions being successfully catalysed by TM-PCs based on the relatively Earth-abundant metals molybdenum[18] and tungsten[19].

As observed for the previously mentioned ATRA reaction and in recent reports on dehalogenation and ring-closing reactions,[53,54] Fe-NHCs show good potential for utility as PCs in the BHAS reaction as well. Especially PC **9** is of interest, due to its beneficial redox potentials ($E°$(Fe(IV)/*Fe(III)) = –1.88 V and $E°$(*Fe(III)/Fe(II)) = 1.0 V vs $Fc^{+/0}$), prolonged excited state lifetime (2 ns, ^{2}LMCT) and absorption in the green region of the visible spectrum.[10] The latter feature is especially beneficial because the employment of lower energy light makes the reaction conditions even more benign than when utilising the previously employed PCs based on molybdenum and tungsten, which absorb blue light. Besides the advantage of potentially avoiding undesirable reactivity, this can aid in the longevity of the catalyst itself.

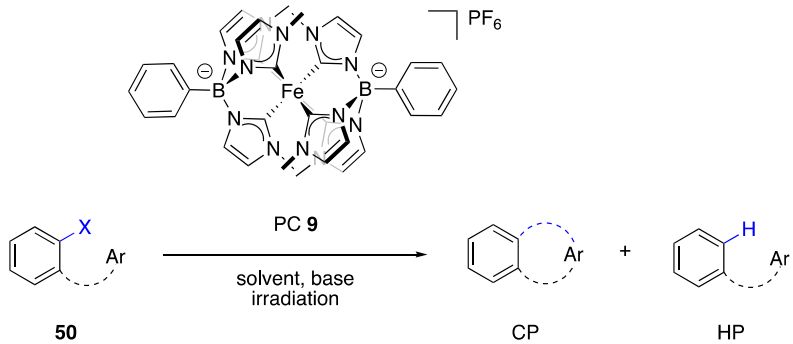

Scheme 9. General overview of the intramolecular visible-light driven BHAS reaction. X = I or Br, Ar = (hetero)aryl.

In that light, investigations were initiated into the employment of Fe-PC **9** to catalyse intramolecular BHAS ring-closing reactions (Scheme 9), which have previously been established to be driven by for example Mo-complex **5** under λ = 450 nm (blue) irradiation.[18] These reactions were tested in the same photocatalytic setup **D** as previously utilised for the ATRA reaction, in presence of PC **9** in 6 mL crimp vials under λ = 530 nm (green) irradiation and argon atmosphere.

3.2 Reaction optimisations

It is worth noting that although the reference reaction system[18] exclusively leads to the cyclised product (CP), the application of the same reaction conditions in case of Fe-PC **9**, in presence of tributylamine (Bu_3N) as a SED, leads to the formation of a mixture of CP and the hydrogen addition product (HP). The latter is also commonly referred to as the hydrodehalogenated or dehalogenated product. The formation of CP is preferred from a synthetic perspective, as for example both the 6*H*-benzo[*c*]chromene[62] and pyrrolo[2,1-*a*]isoquinoline[63] moieties can be found in pharmaceutical and natural products, such as pulchrol and lamellarin I, respectively (Figure 13). Furthermore, various protocols for the generation of HP via the dehalogenation of iodoarenes have been previously established.[16,54,64]

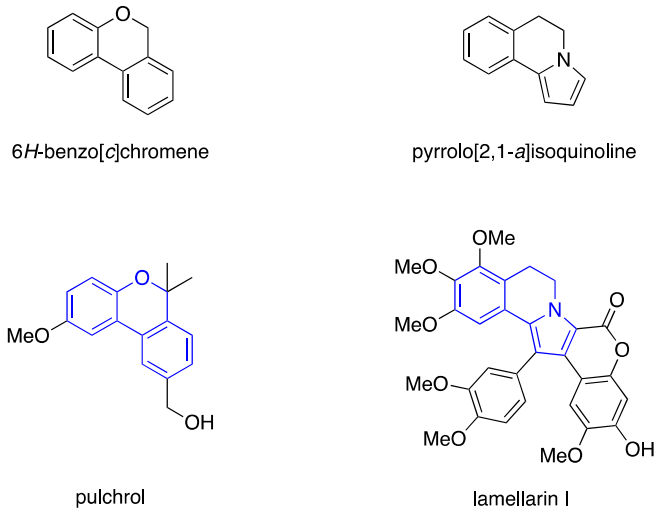

Figure 13. The 6*H*-benzo[*c*]chromene and pyrrolo[2,1-*a*] isoquinoline scaffolds (top) and examples of corresponding natural products (bottom), containing the beforementioned scaffolds.

The optimised reaction conditions for the transformation of **51** to CP-**51** and HP-**51** were initially established to be the following: 50 mM of substrate **51**, 2 mol% of PC **9**, Bu_3N (2 equiv), TMP (2,2,6,6-tetramethylpiperidine, 2 equiv), DMSO-d_6 (2 mL), 48 h of green LED irradiation (λ = 530 nm, 3.03 W/vial) (Table 7, entry 1). These conditions led to full conversion of substrate **51** to CP-**51** and HP-**51**, with a product ratio of 75:25. The product ratio and conversion was determined by ^{1}H NMR analysis of the crude mixture, in which the benzylic signal for the starting material is integrated against the two individual benzylic product signals. Subsequently, a variety of control reactions were performed (Table 7, entry 2–9). A reaction time of 48 h was necessary for the starting material to fully convert (entry 1 and 2). The addition of PC **8** ($[Fe(III)(btz)_3]^{3+}$) instead of PC **9** did not result in any conversion (entry 3). Testing of other Fe-salts and Fe-complexes such as $FeBr_2$ and $[Fe(bpy)_3]^{2+}$ did not lead to any conversion of the starting material either (entry 4 and 5). Employment of the archetypal PC **2** ($[Ru(bpy)_3]^{2+}$), led to the formation of 32% CP-**51** and 22% HP-**51** after 24 h of irradiation (entry 6). Absence of PC, base or irradiation did not result in any conversion (entry 7–9).

Table 7. Control reactions of the BHAS reaction using 50 mM substrate **51** in DMSO-d_6 and 2 mol% PC under green irradiation and inert atmosphere.

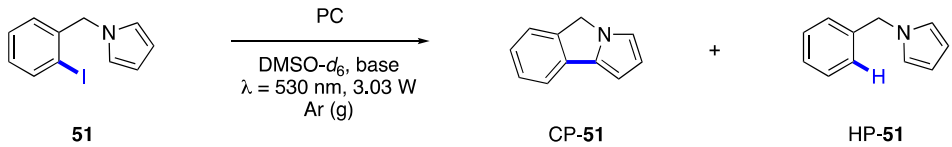

51 CP-**51** HP-**51**

Entry	PC	Base system	Reaction time	Conversion (^{1}H NMR)
1	PC **9**	Bu_3N–TMP (2:2 equiv)	48 h	75% CP: 25% HP
2	PC **9**	Bu_3N–TMP (2:2 equiv)	24 h	65% CP: 17% HP
3	PC **8**	Bu_3N–TMP (2:2 equiv)	24 h	-
4	$FeBr_2$	Bu_3N–TMP (2:2 equiv)	24 h	-
5	$[Fe(bpy)_3]^{2+}$	Bu_3N–TMP (2:2 equiv)	24 h	-
6	PC **2**	Bu_3N–TMP (2:2 equiv)	24 h	32% CP: 22% HP
7	-	Bu_3N–TMP (2:2 equiv)	24 h	-
8	PC **9**	-	24 h	-
9	PC **9**	Bu_3N–TMP (2:2 equiv)	24 h (no irradiation)	-
10	PC **9**	Bu_3N–K_2CO_3 (1:2 equiv)	48 h	83% CP: 17% HP
11	-	Bu_3N–K_2CO_3 (1:2 equiv)	48 h	-
12	PC **8**	Bu_3N–K_2CO_3 (1:2 equiv)	48 h	-
13	PC **2**	Bu_3N–K_2CO_3 (1:2 equiv)	48 h	35% CP: 15% HP

The same reaction conditions were subsequently applied to substrate **52**, which provided a near-full conversion of 96% upon 48 h of irradiation (53% CP-**52** and 43% of HP-**52**) (Table 8, entry 1). This warranted the further optimisation of the dual base system to 1 equiv of Bu_3N and 2 equiv of K_2CO_3, which enhanced the product ratio to 74% of CP-**52** and 26% of HP-**52** (entry 2). Applying these newly found conditions to substrate **51** gave an improved product ratio of 83% CP-**51** and 17% HP-**51** (Table 7, entry 10). Further control reactions were subsequently performed, which again showed no reactivity in absence of PC **9** (entry 11) or if PC **9** was exchanged for Fe-NHC PC **8** (entry 12). The new base system did not significantly influence the reactivity of Ru-PC **2** (entry 13 vs entry 6), and moderate conversions were obtained for both dual base systems.

Table 8. Control reactions of the BHAS reaction using 50 mM substrate **52** in DMSO-d_6 and 2 mol% PC under green irradiation and inert atmosphere.

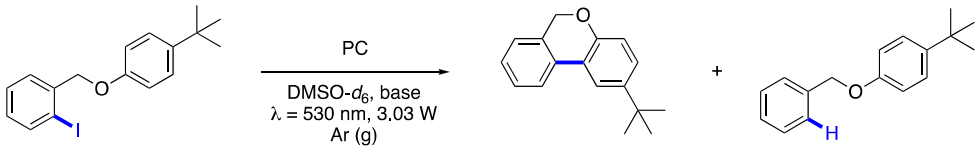

52 CP-**52** HP-**52**

Entry	PC	Base system	Reaction time	Conversion (^{1}H NMR)
1	PC **9**	Bu_3N–TMP (2:2 equiv)	48 h	53% CP: 43% HP
2	PC **9**	Bu_3N–K_2CO_3 (1:2 equiv)	48 h	74% CP: 26% HP
3	PC **9**	Bu_3N–K_2CO_3 (1:2 equiv)	22 h	14% CP: 7% HP
4	-	Bu_3N–K_2CO_3 (1:2 equiv)	48 h	-
5	PC **9**	Bu_3N–K_2CO_3 (1:2 equiv)	48 h (no irradiation)	-
6	PC **9**	-	48 h	-
7	PC **9**	K_2CO_3 (2 equiv)	48 h	-
8	PC **9**	Bu_3N (1 equiv)	48 h	21% CP: 8% HP
9	PC **9**	Bu_3N (3 equiv)	48 h	57% CP: 34% HP
10	PC **8**	Bu_3N–K_2CO_3 (1:2 equiv)	48 h	-
11	$FeBr_2$	Bu_3N–K_2CO_3 (1:2 equiv)	48 h	-
12	$[Fe(bpy)_3]^{2+}$	Bu_3N–K_2CO_3 (1:2 equiv)	48 h	-
13	PC **2**	Bu_3N–K_2CO_3 (1:2 equiv)	48 h	37% CP: 17% HP
14	PC **9**	Bu_3N–K_2CO_3 (1:2 equiv)	48 h (TEMPO (3 equiv) added)	7% CP: 13% HP

Control reactions were performed for substrate **52** as well (Table 8), giving largely the same results as previously observed for the BHAS reaction on substrate **51**. An irradiation time of 48 h was necessary for full conversion (entry 2 and 3). No conversion was observed in absence of PC, bases, or irradiation (entry 4–6). Addition of exclusively 2 equiv of K_2CO_3 and no Bu_3N, did not lead to any conversion either, highlighting the importance of Bu_3N (entry 7). Addition of 1 equiv of Bu_3N, and no K_2CO_3, gave 29% conversion (21% CP and 8% HP) (entry 8). In presence of 3 equiv of Bu_3N, 91% conversion was observed (57% CP and

34% HP) (entry 9). It can therefore be concluded that Bu_3N is key for this reaction to proceed, however, these reaction conditions worsen the product ratio (57% CP and 34% HP). Other Fe-PCs, such as PC **8**, $FeBr_2$ and $[Fe(bpy)_3]^{2+}$ were not able to catalyse the reaction. The addition of PC **2** resulted in minor conversion (Table 8, entry 13), which is very similar to the previous observation in the case of substrate **51** (Table 7, entry 13). Addition of 3 equiv of TEMPO severely hampered the reactivity, and provided just 20% of conversion (Table 8, entry 14), meaning there is a high probability of a radical pathway being present in the reaction mechanism.

These findings illustrate that this specific Bu_3N–K_2CO_3 dual base system is beneficial to not only drive this reaction to completion, but also to favour the formation of CP over HP. It was surprising that DMSO-d_6 was necessary for optimal results, as non-chlorinated solvents generally induce poor cage escape yields for PC **9**.[54] A poor cage escape yield can facilitate charge recombination, which means that the electron transferred from or to the ES easily can return to or from the oxidised or reduced PC, regenerating the PC in its ground state, before the radical intermediate diffuses out of the solvent cage and participates in propagation towards the formation of CP. The use of chlorinated solvents such as DCM (dichloromethane) is associated with larger cage escape yields, which is likely due to a combination of the heavy-atom effect[7] and solvent dielectric effects.[8,54] However, only minor conversion was observed in DCM and the HP formation was favoured over the formation of CP (5% CP-**52** and 10% HP-**52**). The latter could be due to the faster formation of the amine radical cation through reductive quenching of the excited PC **9**, which is hypothesised to assist in the formation of HP. Furthermore, as will be mentioned later in this chapter, it is hypothesised that this reaction mechanism proceeds via various charged intermediates, which is in agreement with a polar solvent being beneficial for product formation.

Another interesting observation is that PC **9** can be employed to catalyse the intramolecular BHAS reaction, whereas the addition of PC **8** does not lead to any conversion of the starting material. In theory, the double excitation mechanism which is operative in the previously discussed ATRA reaction, involving Fe(III)-PC **8** and Fe(II)-PC **7**, should be available under these reaction conditions as well, generating the strongly reducing PC $\mathbf{7}^*$ ($E°(Fe(III)/^*Fe(II))$ = –1.6 V vs $Fc^{+/0}$)[28]. However, neither PC $\mathbf{8}^*$ or PC $\mathbf{7}^*$ is evidently able to reductively cleave the C–I bond. However, as will be discussed later in this chapter, there is no significant oxidative quenching of PC $\mathbf{9}^*$ by the substrate either. The alternative method for initiation of the BHAS reaction would be via the formation of the α-aminoalkyl radical of Bu_3N.[65,66] This would be the result of the initial reductive quenching of either PC $\mathbf{8}^*$ or $\mathbf{9}^*$ by Bu_3N, and subsequent deprotonation of the resulting radical cation $Bu_3N^{\bullet+}$ (or aminium ion). Although both PC $\mathbf{8}^*$ and $\mathbf{9}^*$ exhibit beneficial oxidation potentials ($E°(^*Fe(III)/Fe(II))$ = 1.60 V and 1.0 V vs $Fc^{+/0}$ respectively)[10,27], the reaction is only successfully catalysed in presence of PC **9**.

This difference in reactivity could be due to the significantly shorter excited state lifetime of PC **8*** (100 ps, ^{2}LMCT) compared to PC **9*** (2.0 ns, ^{2}LMCT), potentially making the latter more efficient in the generation of $Bu_3N^{\bullet+}$ under these conditions.

3.3 Substrate scope

Upon optimization of the reaction conditions, a substrate scope was proposed (Figure 14) featuring different scaffolds and various functional groups. These substrates form synthetically valuable cyclised products upon the application of the BHAS reaction conditions. Iodobenzyl-containing substrates were chosen due to the C–I bond being more reactive than the C–Br bond, the former possessing a lower bond dissociation energy than the latter.[67] The majority of the substrates has been functionalised in the para position on the phenyl ring, as it has been previously reported that substitution in that position has the greatest influence on the reactivity.[68] Some substrates feature electron donating groups, such as *tert*-butyl (**52**), methoxy (**53**) or methyl (**54**) substituents, whereas others have been functionalised with electron withdrawing groups, such as aldehyde (**57**), ester (**58**) or trifluoromethyl (**59**) substituents. The results could be interesting since they can be compared to the non-*p*-functionalised substrate **55**. Substrate **56** features a benzyloxy bridge with inverted connectivity, which potentially influences the homolytic bond cleavage of the C–I bond. To confirm the reduced reactivity of the C–Br bond, substrate **60** was included. Substrate **61** was introduced to investigate if the reactivity can be enhanced by introducing the bromo substituent on a naphthalene ring, which has previously been shown to enhance reactivity.[69] To probe if there is an influence of substituents positioned in the para position relative to the C–I bond, both an electron donating (**62**) and electron withdrawing (**65**) group was introduced in that position. Furthermore, the difference in chain length for the pyrrole substrate can be investigated by comparing substrate **51** to **63**. A substrate containing an indole (**64**) moiety was also included to compare its reactivity to its pyrrole analogue (**51**).

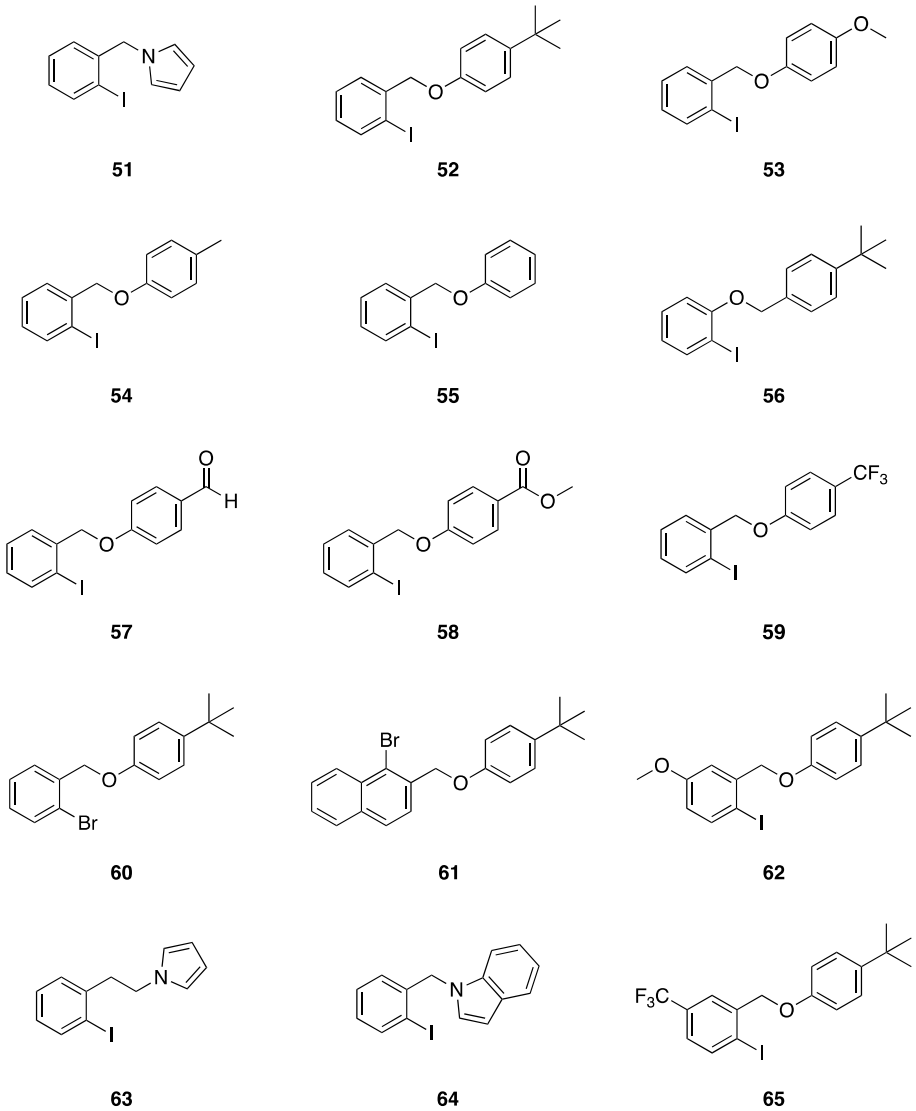

51 **52** **53**

54 **55** **56**

57 **58** **59**

60 **61** **62**

63 **64** **65**

Figure 14. Planned substrate scope for the visible-light driven BHAS reaction.

Table 9. Conversions, product ratios and yields for the BHAS reaction on the different substrates. ^{1}H NMR yields were determined using 1,3,5-trimethoxybenzene as internal standard (IS). n.d. = not determined.

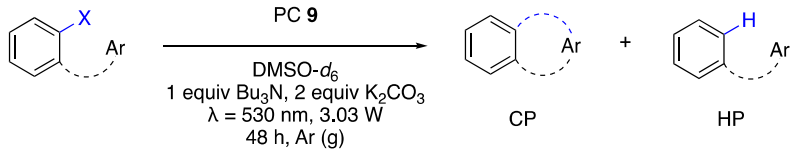

Substrate	Conversion (%)	CP–HP ratio	Yield (^{1}H NMR yield (%), isolated yield (%))	
			CP	HP
51	100	83:17	n.d., 59	n.d., 11
52	100	74:26	53, 46	19, 23
53	100	82:18	58, 35	13, 8
54	100	71:29	52, 26	21, 9
55	95	68:32	55, n.d.	26, n.d.
56	92 (140 h)	77:23	39, n.d.	12, n.d.
59	90	68:32	66, n.d.	10, n.d.
60	0	-	-	-
61	100	87:13	34, 23	5, 3

Table 9 provides the results obtained so far for the different substrates. The model substrates **51** and **52** gave full conversion under the standard reaction conditions and good CP–HP ratios, as determined by ^{1}H NMR analysis of the reaction crude. As will be discussed in the coming section, product isolation has proven challenging, hence leading to moderate isolated yields. Furthermore, for substrates **53** and **54**, also featuring electron donating groups, similar CP–HP ratios and ^{1}H NMR yields were observed. The non-substituted substrate **55** gave a slightly diminished conversion and CP–HP ratio, although the determined ^{1}H NMR yield was quite similar. The substrate containing the benzyloxy bridge with the inverted connection (**56**) exhibited poor reactivity, as 140 h of irradiation was necessary to obtain 92% conversion. Although the CP–HP ratio was quite good in this case, the ^{1}H NMR yields for both CP and HP were rather poor, indicating that the prolonged irradiation time likely has led to the formation of undesired side-products or degradation of the starting material. Substrate **59** features an electron withdrawing group (–CF_3), for which a slightly diminished conversion of 90% was observed in combination with fair ^{1}H NMR yields. For the bromo-substituted substrate (**60**), unsurprisingly, no

conversion was observed. This is in line with the C–Br bond being less reactive than the C–I bond. When employing a bromonaphthalene-containing substrate (**61**) 100% conversion was observed. This is in line with this substrate being more reactive, which is most likely due to the steric hindrance present between Br and H substituents on the naphthalene.[69] However, the poor ^{1}H NMR yields found for CP and HP suggest that other side-products were formed in this reaction. For this substrate, a substantial amount of aldehyde-containing side-product is observed, which will be discussed in a later section of this thesis.

3.4 Product purifications

To irrefutably confirm the formation and identity of the desired products, product isolation and full characterisations (R_f, NMR analyses (^{1}H NMR, ^{13}C NMR, COSY (correlation spectroscopy), HMQC (heteronuclear multiple quantum coherence) and NOESY (nuclear Overhauser enhancement spectroscopy)), HRMS (high-resolution mass spectrometry), EA (elemental analysis) and mp (melting point)) are necessary. However, the separation of CP and HP by customary silica column chromatography proved challenging, as these compounds exhibit nearly identical polarities.

3.4.1 The isolation of CP- and HP-51

Several methods were attempted to isolate CP-**51** and HP-**51** from the crude product mixture. Neither flash silica column chromatography with petroleum ether (PE) as a mobile phase, a Biotage automated flash column system employing a solvent gradient (0 → 10% EtOAc in PE), nor preparative TLC could be employed to provide sufficient product separation. However, a gravitational silica column with PE as eluent gave nearly pure product fractions. Upon drying of the product-containing fractions overnight, sublimation (CP-**51**) and evaporation (HP-**51**) was observed. A controlled vacuum-sublimation of a sample containing predominantly CP-**51** with a cold finger gave analytically pure white crystals of CP-**51** (6.0 mg, 0.04 mmol, 40%). After an additional gravitational silica column (PE) of the remaining fractions containing slightly impure HP-**51**, analytically pure HP-**51** (2.8 mg, 0.02 mmol, 20%) was obtained as a colourless oil.

Attempts to directly vacuum-sublimate CP-**51** from either the crude reaction mixture, or from a mixture of CP-**51** and HP-**51** led to a mixture of both compounds on the cold finger, as apparently simultaneous sublimation and evaporation was occurring.

As the previously discussed purification method was rather extensive, the isolation was adjusted by incorporating a Sephadex LH-20 column (MeOH). This type of column is a combined affinity and size-exclusion chromatography method and was

therefore hypothesised to be effective in separating CP-**51** from the more flexible HP-**51**. Repetition of the isolation on five combined crude reactions by gravitational silica column chromatography (PE), followed by a Sephadex LH-20 column (MeOH), led to the successful isolation of analytically pure fractions of CP-**51** (45.7 mg, 0.29 mmol, 59%) and HP-**51** (8.3 mg, 0.05 mmol, 11%).

3.4.2 The isolation of CP- and HP-52

For the product mixture containing CP-**52** and HP-**52**, a gravitational silica column (PE) was attempted, however, no satisfactory separation was obtained. Similar to the previous product mixture, one of the compounds is an oil (CP-**52**), whereas the other is a solid (HP-**52**). Hence, it was hypothesised that the use of a bulb-to-bulb microdistillation/-sublimation apparatus (also known as a Kugelrohr, Figure 15)[70] could lead to the successful isolation of the individual products. In such a setup, a small amount of the crude mixture is added to a round-bottom flask. Several bulbs are attached to this flask via tapered joints and placed inside of an oven under vacuum and continuous rotation. Slowly raising the temperature inside of the oven allows for the selective sublimation or evaporation of the target compound to the colder collection bulbs situated on the outside of the oven. However, this method proved unsuccessful and no pure products were obtained after several attempts.

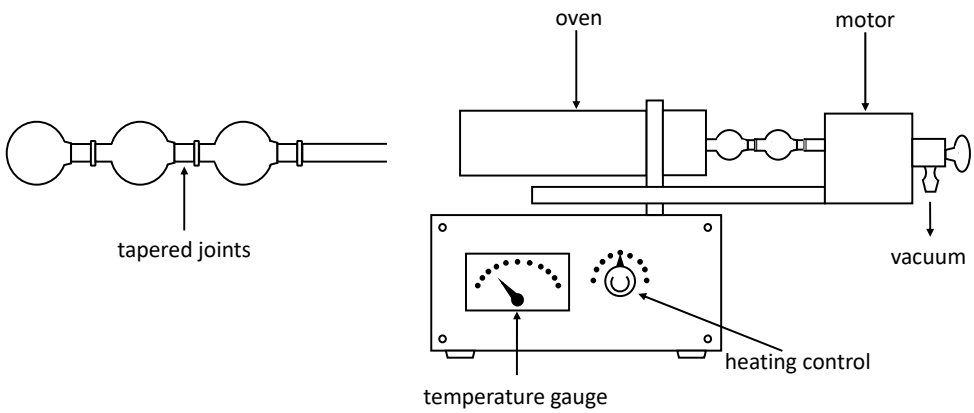

Figure 15. Schematic overview of the Kugelrohr (bulb-to-bulb) microdistillation/-sublimation apparatus. Schematic illustration adapted from ref. 70.

Analysis of the crude product mixture on reverse phase TLC or neutral alumina TLC with various eluents did not indicate sufficient separation either. Repeating the purification on five combined crude product mixtures by flash silica column chromatography (PE), followed by a Sephadex LH-20 column (MeOH), provided analytically pure CP-**52** (55.4 mg, 0.23 mmol, 46%) and HP-**52** (27.4 mg, 0.11 mmol, 23%).

3.4.3 The isolation of CP- and HP-53, 54 and 61.

For the purification of products CP-**53** and HP-**53** (Scheme 10), an initial silica column was performed (1% EtOAc in PE), providing a mixture of CP-**53** and HP-**53** (ratio 80:20). The previously employed Sephadex LH-20 column could not be used in this case, due to poor solubility of the crude mixture in methanol. However, consecutive reverse phase preparative HPLC (high-performance liquid chromatography, MeCN–H_2O, 0.1% formic acid (FA)) purifications of small batches of the product mixture gave analytically pure CP-**53** (40.1 mg, 0.19 mmol, 35%) and HP-**53** (9.2 mg, 0.04 mmol, 8%).

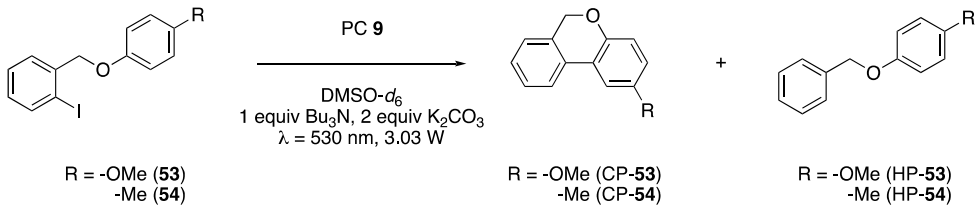

Scheme 10. Additional BHAS reactions featuring -OMe and -Me substituents on the substrates.

CP-**54** and HP-**54** were purified in a similar fashion as the beforementioned CP-**53** and HP-**53**, meaning that five combined reaction crudes were subjected to silica column chromatography (0 → 0.5 % EtOAc in PE), followed by multiple reverse phase preparative HPLC (MeCN–H_2O, 0.1% FA) runs. Analytically pure CP-**54** (25.8 mg, 0.13 mmol, 26%) and HP-**54** (9.0 mg, 0.05 mmol, 9%) were successfully isolated.

CP-**61** and HP-**61** were also purified by a similar method. Four combined reaction crudes were subjected to silica column chromatography (0 → 2 % EtOAc in PE), and numerous consecutive reverse phase preparative HPLC (MeCN–H_2O, 0.1% FA) runs, providing analytically pure CP-**61** (26.9 mg, 0.09 mmol, 23%) and HP-**61** (3.6 mg, 0.01 mmol, 3%).

3.5 Mechanistic investigations

3.5.1 Photophysical investigations

Efforts have been made to elucidate the reaction mechanism (Scheme 11) for the intramolecular BHAS reaction employing PC **9**, Bu_3N and K_2CO_3 in DMSO-d_6 under argon atmosphere and irradiation with green light (λ = 530 nm, 3.03 W/vial). The ES lifetime of PC **9*** was determined to be 1.45 ns in DMSO, which is slightly less than the 2 ns previously determined in acetonitrile. The bimolecular emission

quenching of PC **9*** by various substrates (**51**, **52** and **56**) was probed (Figure 14, Table 10). These substrates were chosen because of their structural variation (**51** (pyrrole containing) vs **52** and **56**) and/or difference in observed reactivity (**51** and **52** vs **56**). The difference in reactivity is mainly evident from the prolonged reaction time needed to fully convert substrate **56** (140 h), whereas just 48 h of irradiation is needed for substrate **51** and **52**.

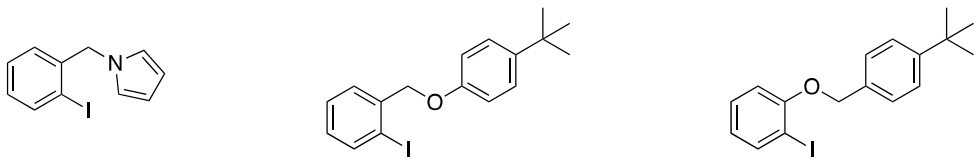

51 **52** **56**

Figure 14. The substrates used for the probing of the oxidative emission quenching of PC **9***.

The Stern–Volmer analysis of the emission quenching studies indicated marginal (**51** and **56**), or no observable (**52**) oxidative quenching between the beforementioned ES and the individual substrates (Table 10). Furthermore, no charge separated products were identified upon oxidative quenching by the substrates, meaning it was not possible to determine a cage escape yield (η_{ce}). Some charge separated products were observed for the quenching by substrate **51**. However, it was not confirmed that these were formed by an oxidative quenching event, as the expected stable Fe(IV) species[71] could not be unambiguously identified from the obtained TA spectra. The subcomponent iodobenzene also showed marginal quenching with no determinable η_{ce}, which is indicative of an initial oxidative quenching process by the substrate being unlikely, and hence in line with the absence of quenching in case of substrate **52**. Because substrate **51** showed the best quenching of the substrates, 1-methylpyrrole and benzylpyrrole were probed as quenchers as well, for which higher quenching rates and η_{ce} values were obtained. It is therefore possible that the pyrrole moiety can participate in unproductive quenching with PC **9***, after which a charge recombination potentially occurs after cage escape. No substantial evidence for the direct productive oxidative quenching of PC **9*** by the substrates was found.

When probing the reductive quenching of **9*** by the SED Bu_3N, a reductive quenching rate was obtained which is in the same order of magnitude as the values obtained for substrates **51** and **56**, but significantly smaller than the k_q obtained for Et_3N. No charge separated products could be detected and hence η_{ce} could not be determined. However, although no oxidative quenching is observed for the model substrate **52**, the reaction seems to proceed in a very similar manner to the other substrates, as can be deduced from the beforementioned product ratios. It is therefore likely that the initial productive SET occurs from the Bu_3N to PC **9***,

thereby generating the PC in the reduced Fe(II) ground state (**9**'). Other competing quenching events that might take place simultaneously are likely unproductive.

Table 10. Determined bimolecular quenching rate constants (k_q) and cage escape yields (η_{ce}) for selected quenchers in DMSO as solvent. n.a. = not available. [a] No observable quenching. [b] Upper limit (no obvious observable signal within detector limit, any available signal is assumed to be less than the lowest observable signal, 0.0010 mOD).

Quencher	Bimolecular quenching rate constant (k_q, $M^{-1} s^{-1}$)	Cage escape yield (η_{ce})
51	$0.66 \cdot 10^9$	0.03
52	–[a]	n.a.
56	$0.11 \cdot 10^9$	n.a.
Iodobenzene	$0.01 \cdot 10^9$	n.a.
1-Methylpyrrole	$1.95 \cdot 10^9$	0.02
Benzylpyrrole	$0.99 \cdot 10^9$	0.02
Bu_3N	$0.44 \cdot 10^9$	< 0.04[b]
Et_3N	$2.58 \cdot 10^9$	0.02

3.5.2 Proposed mechanism

The reaction is suggested to be initiated by the reductive quenching of PC **9*** by Bu_3N. This generates Fe(II)-species **9**' and the $Bu_3N^{\bullet+}$ radical cation in the process (Scheme 11). The α-aminoalkyl radical **A** is formed by the deprotonation of the $Bu_3N^{\bullet+}$ radical cation and can participate in either SET or XAT with the substrate **B**.[65,66] Depending on the mode of action, the iminium cation **D** is either formed directly, or, in the case of XAT, via intermediate **C**.

The phenyl radical intermediate **E** can then abstract an electron and a proton, either consecutively, or simultaneously via hydrogen atom transfer (HAT) to form HP. Intermediate **E** can instead proceed to ring-close, forming the reactive cyclised intermediate **F**. Subsequently, single electron oxidation leads to the formation of the cationic intermediate **G**, after which deprotonation leads to the desired CP.

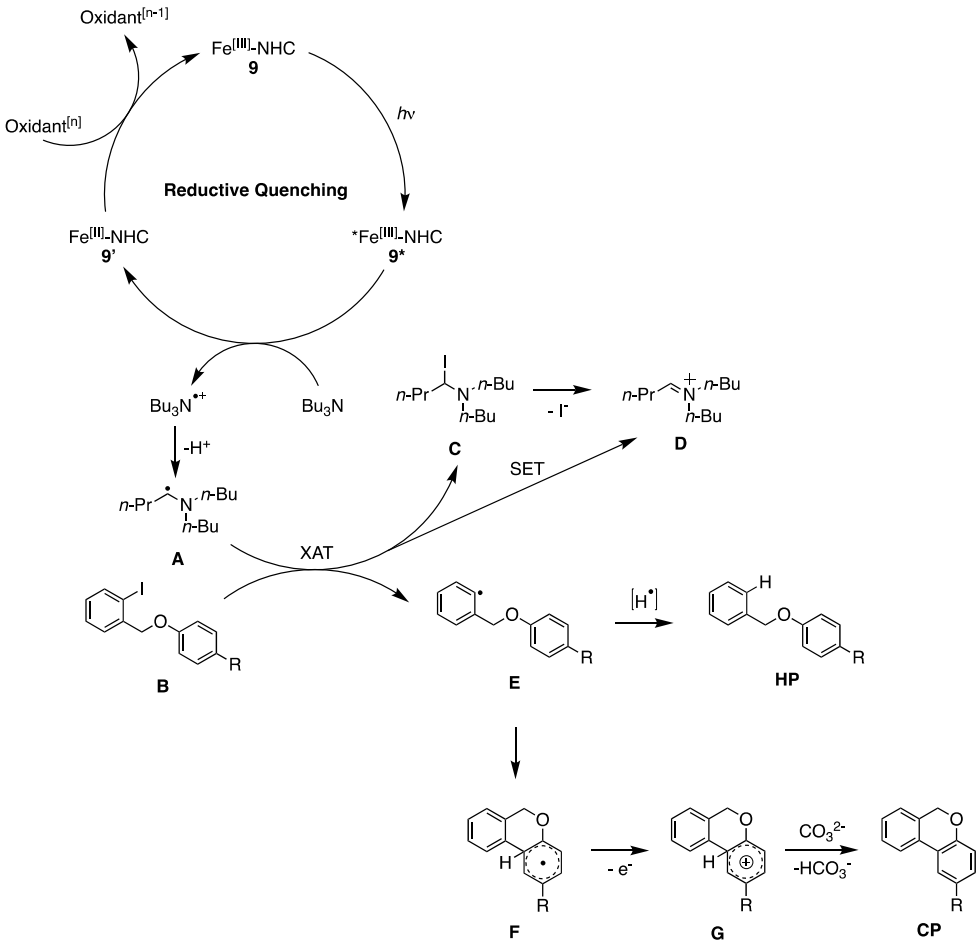

Scheme 11. Proposed reaction mechanism for the BHAS reaction employing PC **9**.

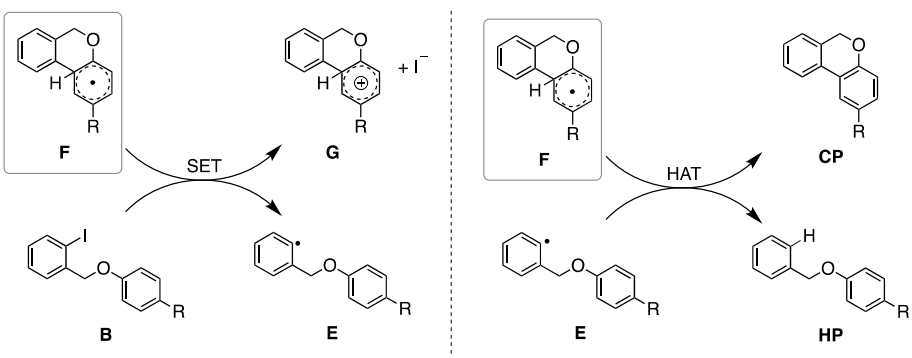

Scheme 12. Proposed radical chain propagation pathways for the BHAS reaction.

Although it has been previously established that the $Bu_3N^{\bullet+}$ radical cation can assist in the formation of HP,[72] such a process is less likely to be operative here, as full conversion is observed in presence of just 1 equiv of Bu_3N. Because Bu_3N first reduces $\mathbf{9}^*$, and subsequently is involved in the reduction of substrate **B**, it is not able to provide the necessary electron needed in the formation of HP. It is more likely that a radical chain propagation pathway is operative (Scheme 12, right), in which HP and CP are formed simultaneously. Alternatively, a deprotonation from the $Bu_3N^{\bullet+}$ radical cation occurs in combination with the oxidation of the Fe(II) $\mathbf{9}'$ species, which leads to the formation of HP. To confirm whether Bu_3N is the proton source for the formation of HP, 1 equiv of fully deuterated Bu_3N was added to the reaction mixture instead of Bu_3N. However, this inhibited the reactivity of the reaction system. The impaired reactivity is in line with a kinetic isotope effect (also named deuterium isotope effect),[73] which supports that the deprotonation to form the α-aminoalkyl radical **A** is a key step in the initiation of the reaction. Furthermore, it supports that α-aminoalkyl radical **A** is the most likely species to induce the homolytic cleavage of the C–I bond of substrate **B**. However, once the reaction has initiated, a radical chain propagation pathway (Scheme 12, left), is likely to be at play, in which the cyclised radical intermediate **F** could participate in SET with substrate **B**.

Additionally, lowering the amount of Bu_3N to 0.5 equiv gave full conversion in case of the model substrate **52**, corroborating the presence of a radical propagation pathway, as intermediate **A** is evidently necessary for the reaction to initiate. Further reduction of the amount of added Bu_3N to 0.2 equiv gave 42% conversion, which is higher than the theoretical conversion that could be obtained in case of an equimolar process. In combination with the observation of the addition of TEMPO (3 equiv) hampering the reactivity to 20% conversion, this suggests the presence of at least one radical chain propagation pathway in the mechanism.

The rather long reaction times could be attributed to a low quantum yield of Φ = 0.003–0.004, as determined by chemical actinometry. This is in line with the low quenching rates previously mentioned for the reductive quenching of PC $\mathbf{9}^*$. Raising the efficiency of quenching by adding for example TEA instead of Bu_3N as SED, or exchanging of the DMSO solvent for acetonitrile, worsened the CP–HP ratio. A potential reason for this can be that the steady state concentration of **E** and **F** are raised in case of improved quenching. This would allow for the radical propagation pathway (Scheme 12, right) to proceed more efficiently, hence generating more HP in the process towards CP. By keeping the concentration of the α-aminoalkyl radical **A**, and therefore **E**, low, the reaction is allowed to proceed towards CP without forming extensive amounts of HP in the process. This is also a possible reason for why 3 equiv of Bu_3N gives worse results than if 1 equiv of Bu_3N is added in combination with 2 equiv of K_2CO_3. The rather long reaction times therefore appear to be necessary for this reaction to proceed with the best possible CP–HP ratio.

3.6 Aldehyde side-product

Interestingly, for the BHAS reaction substrates containing the benzyloxy moiety, an aldehyde side-product (AP) could be identified upon completion of the reaction, besides the expected CP and HP (Table 11). The presence of such an AP side-product was mainly evident from a characteristic aldehyde peak around 10 ppm in the ^{1}H NMR. The ^{1}H NMR ratios were determined by integration of the characteristic benzylic (CP and HP) and aldehyde (AP) signals in the crude ^{1}H NMR, correcting for the number of nuclei for the respective signals, and subsequent division by the sum of the corrected integrals.

Table 11. ^{1}H NMR ratios of CP, HP and AP for the different substrates under BHAS reaction conditions.

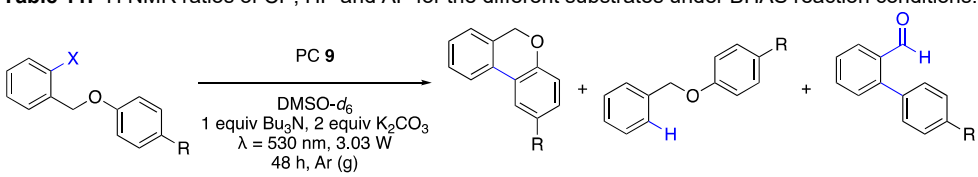

X = I or Br
R = electron donating substituent or H

CP HP AP

Substrate	Conversion (%)	^{1}H NMR ratio (%)		
		CP	HP	AP
52	100	66	23	11
53	100	70	16	14
54	100	64	28	8
55	95	65	29	6
61	100	44	7	49

For example, the formation of AP-**53**, AP-**54** and AP-**61** from the corresponding substrate **53**, **54** and **61** was observed under the BHAS reaction conditions (Table 11). These side-products were successfully isolated by either flash silica column chromatography or preparative reverse phase HPLC. ^{1}H NMR spectra (see Appendix) were recorded for the purified AP-**53** and AP-**54**, which were in accordance with previously published data.[74,75] The ^{1}H NMR spectrum for AP-**61** has not been reported previously in literature, however, the obtained spectrum bears a large resemblance to a reported ^{1}H NMR spectrum on a structural analogue, containing a methyl instead of a *tert*-butyl substituent.[76]

The formation of the AP side-product has only been observed in presence of electron donating substituents (–^{t}Bu, –OMe and –Me) (substrate **52**, **53**, **54** and **61**)

positioned in the para position relative to the bridging oxygen (Table 11), or, to a lesser extent, in absence of substituents (substrate **55**) In presence of electron withdrawing groups in the same position, such as an ester (–COOMe) or trifluoromethyl ($–CF_3$) group (substrate **58** and **59**), no AP formation was observed.

A proposed mechanism for the formation of AP is shown in Scheme 13. The pathway is initiated by the formation of the reactive intermediate **E**. This initiation step is the same as has been shown before in Scheme 11 for the general BHAS mechanism. However, for the formation of the AP side-product, a 5-*exo* cyclisation is proposed to take place, instead of the traditionally observed 6-*endo* cyclisation, which is hypothesised to lead to the formation of CP (Scheme 14). An earlier report on BHAS reactions has investigated the 5-*exo* and 6-*endo* cyclisation pathways by molecular modelling calculations.[68] It was theoretically determined that the transition state for the 5-*exo* cyclisation is higher in energy than in case of the 6-*endo* cyclisation.[68] However, the 5-*exo* pathway leads to a radical intermediate which is energetically more favourable than the intermediate formed after the alternative 6-*endo* ring-closure.[68]

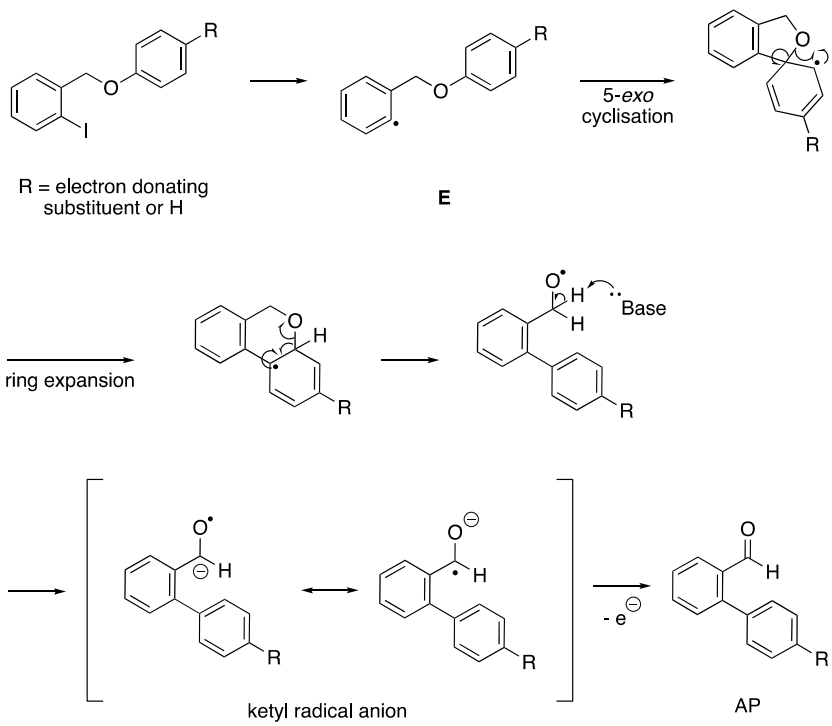

Scheme 13. Proposed photoinduced formation pathway of AP.

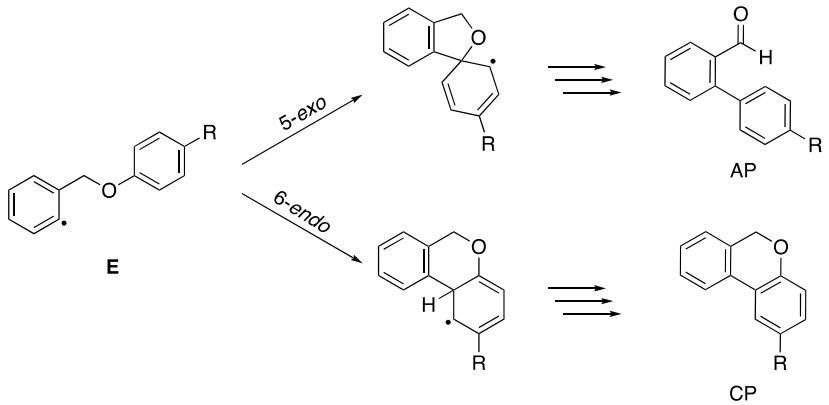

Scheme 14. Schematic overview of the possible 5-exo and 6-endo cyclisations from radical intermediate **E** to form AP and CP, respectively.

Potentially, the 5-*exo* pathway is more accessible and relatively lower in energy for substrates containing electron donating substituents, whereas it is not accessible for those containing electron withdrawing substituents. The 6-*endo* pathway appears to be accessible regardless of the electron donating or withdrawing nature of the substituents on the substrates, allowing for the formation of CP. For substrate **61**, the 5-*exo* and 6-*endo* transition states are potentially similar in energy, allowing for the nearly equal formation of CP-**61** and AP-**61** (Table 11).

The formation of AP is proposed to continue from the 5-*exo* cyclised radical intermediate by a ring expansion and ring opening step (Scheme 13). Subsequently, a deprotonation results in the generation of a ketyl radical anion. This intermediate is stabilised by resonance in which the adjacent aromatic system can participate. In the final step of the proposed mechanism, the ketyl radical anion is oxidised ($E_{1/2}$(benzaldehyde/benzaldehyde$^{\bullet-}$) = –2.31 V vs $Fc^{+/0}$, reported as –1.93 V vs SCE)[45,77], forming the experimentally observed AP.

The utilisation of such a photoinduced reaction pathway to generate aldehydes, to the best of our knowledge, is not known in literature. The formation of these aldehyde products and the corresponding mechanistic investigations could therefore be interesting targets for future investigations.

3.7 Conclusion

Fe-NHC PC **9** was successfully employed to catalyse the BHAS reaction driven by green light for a variety of substrates. A dual base system of Bu_3N–K_2CO_3 (1:2 equiv) was employed to optimise the ratio of CP formation over HP formation. Furthermore, DMSO was found to be the optimal solvent for this reaction. However, even when employing the established optimised reaction conditions, the reaction times are rather long (48 h).

A mechanism was proposed in accordance with the experimental observations for the substrates and mechanistic investigations, which included various methods grounded in either synthetic organic or physical chemistry. One of the main findings was the key role of the Bu_3N in the initiation of the photocatalytic reaction. The initial hypothesis was the direct oxidative quenching of PC **9*** by the substrates, however, as no fluorescence quenching was spectroscopically observed for the benchmark substrate **52**, reductive quenching of PC **9*** by Bu_3N is more likely to be the initial step under these reaction conditions.

It is noteworthy that the improvement of the initial quenching step by either altering the quencher or solvent led to a poorer CP–HP ratio. This implies that the improvement in the ratio of CP–HP formation happens at the expense of overall reactivity of the system.

Another interesting finding was the lack of reactivity of PC **8** in this reaction, as these reaction conditions also should allow for the double excitation previously observed in the ATRA reaction. However, this could be due to the significantly lower ES lifetimes of PC **8** (and PC **7**) compared to PC **9**.

Despite the challenging isolation of the various products for each reaction mixture, this report is valuable in contributing to the body of knowledge on iron photoredox catalysis. Furthermore, this is an alternative way of driving the BHAS reaction under even milder conditions, such as the use of green light irradiation and the K_2CO_3 base, instead of blue light and ^{t}BuOK. This allows for the presence of otherwise sensitive substituents on the substrates, such as aldehyde or ester moieties, which are otherwise not tolerated.

Future efforts should be dedicated to the completion of the isolation of the various reaction products as well as the further exploration into the formation of AP.

4 Conclusion and outlook

The prolonged ES lifetimes in the ps–ns region, green light absorption and beneficial redox potentials have made Fe-NHC iron complexes interesting targets for investigation as Earth-abundant PCs under irradiation with visible light. In this thesis, two examples of the successful application of such PCs have been discussed.

Firstly, various photoreactor setups were probed in the investigation of the ATRA reaction. This reaction was successfully catalysed by PC **9** under lower irradiation intensities, albeit with longer reaction times. However, under irradiation with blue light, PC **9** was outperformed by a background reaction. Further investigations led to the interesting discovery of PC **8** being able to efficiently catalyse the reaction either directly, or through a double excitation mechanism also involving Fe(II)-PC **7**. A broad substrate scope was established and a mechanism was proposed for both the reductive and oxidative quenching pathways. These findings illustrate the utility of Fe-NHC PCs **7** and **8**, despite featuring sub-ns ES lifetimes.

Subsequently, the performance of Fe-NHC complexes **7**, **8** and **9** as PCs in the BHAS reaction was investigated. It was found that PC **9** was able to drive the BHAS reaction under mild conditions in presence of green light. Further reaction optimisations showed the necessity for the Bu_3N–K_2CO_3 (1:2 equiv) dual base system to obtain the best possible CP–HP ratio. A substrate scope was established and a protocol for the isolation of the various products was developed. Mechanistic investigations showed that this reaction most likely proceeds under reductive quenching conditions. Furthermore, the formation of AP was investigated and discussed.

Interestingly, PC **7** and **8** were able to efficiently catalyse the ATRA reaction, whereas they did not show any reactivity in the BHAS reaction, where PC **9** was found to be the preferred catalyst. PC **7** and **8** exhibit shorter ES lifetimes compared to PC **9**, however, the latter suffers from poor cage escape yields in non-chlorinated solvents. This could be the reason for why PC **9** was not sufficiently reactive in the ATRA reaction, whereas the ES lifetime potentially plays a bigger role in the BHAS reaction, where a poor cage escape yield is evidently tolerated.

The number of examples of Fe-PCs being successfully applied in photoredox chemistry is still rather low and further investigation into their mode of action could prove beneficial to the research field. Furthermore, the implications of the ^{2}LMCT state on photoredox catalytic reactivity is worth further investigations as well.

5 Acknowledgements

I would like to express my gratitude to all of those that have, in some way or another, supported or helped me during my PhD.

First and foremost, I would like to thank **Kenneth** for giving me the opportunity to pursue a PhD in the KW group and work on a novel and very interesting project. I have learnt a lot during my years here and I am appreciative of everything you have done for me.

Thank you, **Ola** (my co-supervisor) and **Ulf N.** (my department representative), for the feedback and discussions we have had, especially during my ISP meetings and half-time seminar. I also want to express my gratitude to **Ulf E.** and **Sophie** for being supportive of me during my PhD.

I would also like to thank the KW group, all past and present members, for your support, scientific discussions and, not to forget, the fun times we have had. **Valtýr**, you have been there for me from the beginning, and I wish you the best of luck with the writing of your thesis. **Anna**, we ended up writing our theses together, which was really helpful for me, I hope that it was helpful for you too. I have enjoyed working with you all these years, and I am very much looking forward to your defence. **Samuel**, I have enjoyed working alongside you in the lab and office, and it was nice attending the Cancún conference with you. **Abhishek**, good luck with the rest of your postdoc. **Eric** and **Clara**, I wish you the best of luck with the continuation of your PhD studies.

Furthermore, I would like to thank those that have been involved in the photoredox catalysis project with me. **Simon**, thank you so much for guiding and supporting me in the beginning of my PhD. **Aleks** and **Jesper**, you have done amazing work on the ATRA reaction. I also appreciate the discussions we have had; they were very helpful, and I have learnt a lot. Also, a special thanks to **Jesper** for proofreading my thesis. **Alpesh**, thank you for your work on the BHAS reaction. **Catherine** and **Reiner**, thank you for the collaborations on the photoredox catalysis projects and fruitful discussions we have had.

I would also like to thank those at Chemical Physics, who I have had the chance to meet during the first years of my PhD. A special thank you to **Jens**, for designing the first photoreactor that I have used. **Linnea**, **Pavel** and **Nils**, I have really enjoyed

discussing the iron carbenes with you, although we sadly never got the chance to collaborate.

Maria, **Sara**, and **Kornelije**, thank you for everything you have done for me during my stay at CAS. **Katarina** and the others at **KC purchasing**, thank you for all of the help with my (sometimes difficult) orders of chemicals and equipment.

Sofia, **Annette** and **Fiona**, thank you for the running of HRMS samples.

Thank you to those I have worked with in lab A, and a special thanks to **Alexander**, **Tiago**, **Daniel**, **Mujtaba**, **Roberto**, **Fredrik** and **Joachim** for all of the assistance I have received with the LC-MS and prep HPLC.

Of course, a big thank you to all the past and present members of CAS, for the nice time I have had working here and for all of the nice discussions we have had. Thank you to those I have taken PhD courses with, and those I have had the chance to teach with.

Thank you to all of my friends, who have supported me during my time as a PhD student, especially **Tommy**, for the board game nights and for making the front cover of my thesis!

Mama, **papa** en **Ilona**, dank jullie wel voor alle steun. Het was niet altijd even makkelijk, maar ik heb het gered! Tack **Josefine** och **Peter** och resten av familjen för ert stöd och all hjälp jag och Fredrik har fått under dessa år!

Sist men absolut inte minst, tack **Fredrik**. Jag kan med all säkerhet säga att jag inte hade klarat det utan dig. Jag älskar dig och jag älskar vår lilla familj.

6 Appendix

6.1 Characterisations of aldehyde compounds discussed in chapter 3

6.1.1 4'-Methoxy-[1,1'-biphenyl]-2-carbaldehyde (AP-53)

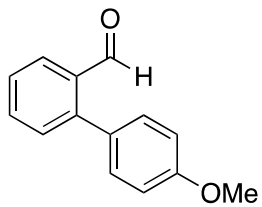

^{1}H NMR (500 MHz, $CDCl_3$, δ) 10.00 (s, 1H), 8.01 (dd, *J* = 7.9, 1.5 Hz, 1H), 7.62 (td, *J* = 7.5, 1.5 Hz, 1H), 7.48 – 7.43 (m, 2H), 7.33 – 7.28 (m, 2H), 7.05 – 6.96 (m, 2H), 3.88 (s, 3H) ppm. In accordance with literature spectrum.[75]

6.1.2 4'-Methyl-[1,1'-biphenyl]-2-carbaldehyde (AP-54)

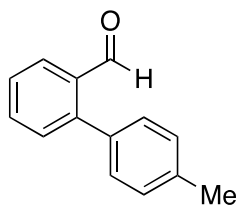

^{1}H NMR (400 MHz, $CDCl_3$, δ) 9.99 (s, 1H), 8.02 (dd, *J* = 7.8, 1.4 Hz, 1H), 7.63 (td, *J* = 7.5, 1.5 Hz, 1H), 7.50 – 7.43 (m, 2H), 7.28 (s, 4H), 2.44 (s, 3H) ppm. In accordance with literature spectrum.[75]

6.1.3 1-(4-(*tert*-Butyl)phenyl)-2-naphthaldehyde (AP-61)

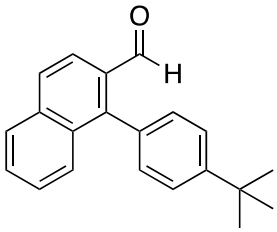

^{1}H NMR (400 MHz, $CDCl_3$, δ) 9.90 (d, *J* = 0.9 Hz, 1H), 8.06 (d, *J* = 8.7 Hz, 1H), 7.94 – 7.91 (m, 2H), 7.74 – 7.71 (m, 1H), 7.64 – 7.60 (m, 1H), 7.56 – 7.54 (m, 2H), 7.49 – 7.45 (m, 1H), 7.35 – 7.33 (m, 2H), 1.43 (s, 9H).

6.2 NMR spectra of aldehyde compounds discussed in chapter 3

6.2.1 ^{1}H NMR spectrum of AP-53

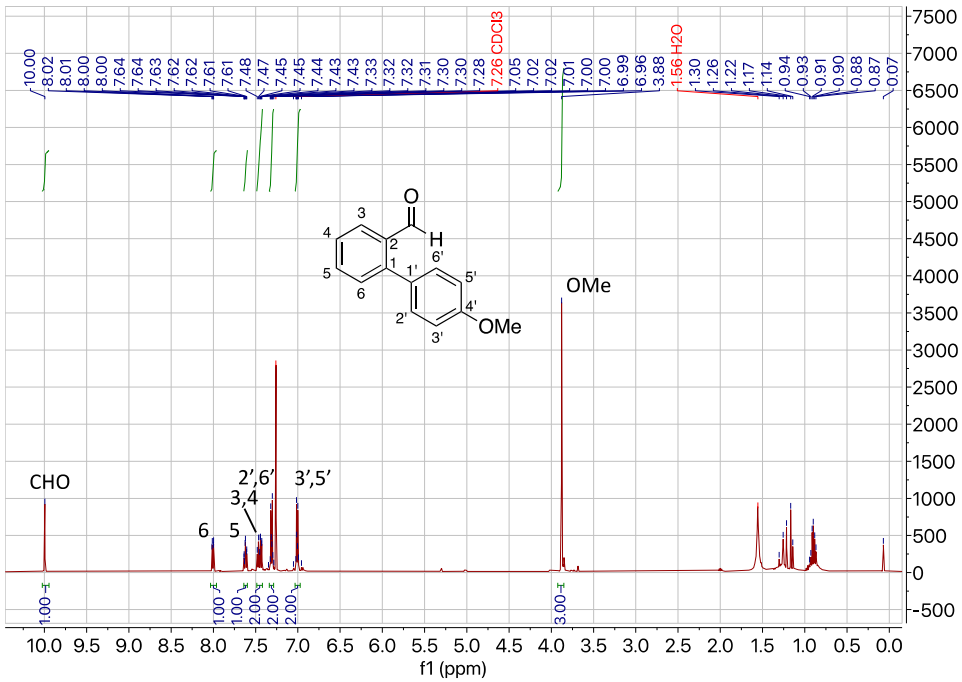

6.2.2 ^{1}H NMR spectrum of AP-54

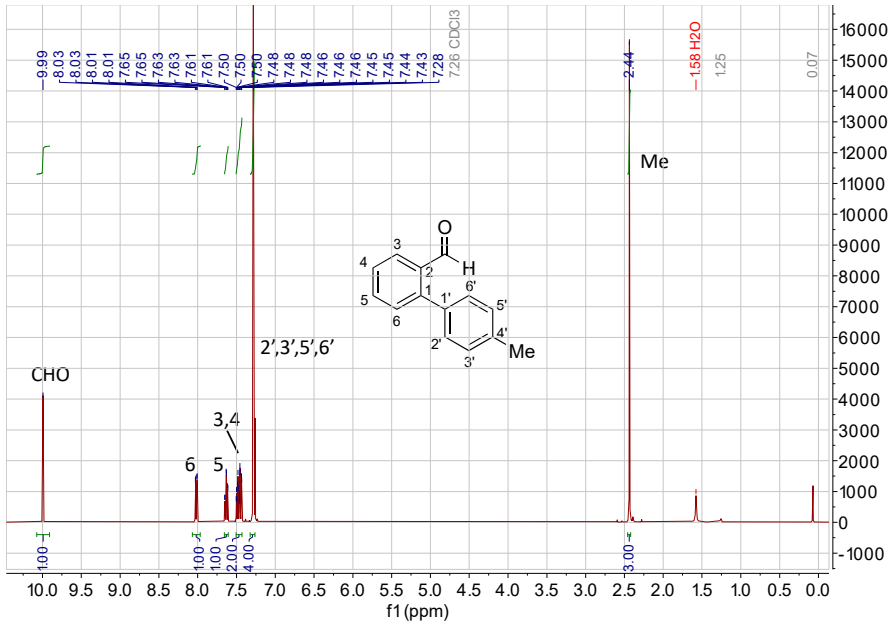

6.2.3 ^{1}H NMR spectrum of AP-61

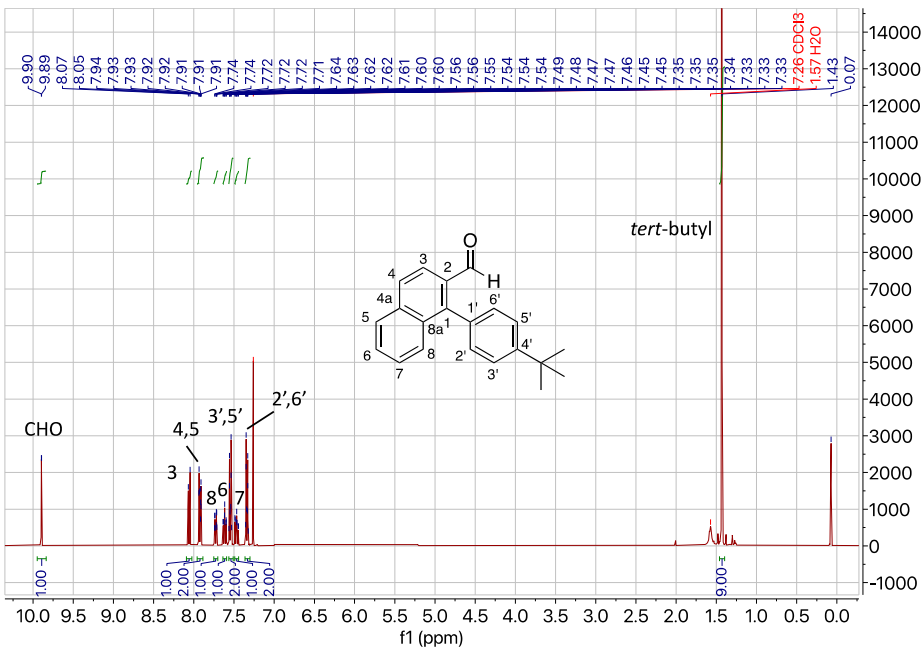

7 References

(1) Marzo, L.; Pagire, S. K.; Reiser, O.; König, B. Visible-Light Photocatalysis: Does It Make a Difference in Organic Synthesis? *Angew. Chemie Int. Ed.* **2018**, *57* (32), 10034–10072.

(2) Prier, C. K.; Rankic, D. A.; MacMillan, D. W. C. C. Visible Light Photoredox Catalysis with Transition Metal Complexes: Applications in Organic Synthesis. *Chem. Rev.* **2013**, *113* (7), 5322–5363.

(3) Cheung, K. P. S.; Sarkar, S.; Gevorgyan, V. Visible Light-Induced Transition Metal Catalysis. *Chem. Rev.* **2022**, *122* (2), 1543–1625.

(4) Schultz, D. M.; Yoon, T. P. Solar Synthesis: Prospects in Visible Light Photocatalysis. *Science* **2014**, *343* (6174), 1239176–1239176.

(5) Romero, N. A.; Nicewicz, D. A. Organic Photoredox Catalysis. *Chem. Rev.* **2016**, *116* (17), 10075–10166.

(6) Arias-Rotondo, D. M.; McCusker, J. K. The Photophysics of Photoredox Catalysis: A Roadmap for Catalyst Design. *Chem. Soc. Rev.* **2016**, *45* (21), 5803–5820.

(7) Olmsted, J.; Meyer, T. J. Factors Affecting Cage Escape Yields Following Electron-Transfer Quenching. *J. Phys. Chem.* **1987**, *91* (6), 1649–1655.

(8) de Groot, L. H. M.; Ilic, A.; Schwarz, J.; Wärnmark, K. Iron Photoredox Catalysis–Past, Present, and Future. *J. Am. Chem. Soc.* **2023**, *145* (17), 9369–9388.

(9) Balzani, V.; Bergamini, G.; Campagna, S.; Puntoriero, F. Photochemistry and Photophysics of Coordination Compounds: Overview and General Concepts. In *Photochemistry and Photophysics of Coordination Compounds I*; Springer Berlin Heidelberg: Berlin, Heidelberg; pp 1–36.

(10) Kjær, K. S.; Kaul, N.; Prakash, O.; Chábera, P.; Rosemann, N. W.; Honarfar, A.; Gordivska, O.; Fredin, L. A.; Bergquist, K.-E.; Häggström, L.; Ericsson, T.; Lindh, L.; Yartsev, A.; Styring, S.; Huang, P.; Uhlig, J.; Bendix, J.; Strand, D.; Sundström, V.; Persson, P.; Lomoth, R.; Wärnmark, K. Luminescence and Reactivity of a Charge-Transfer Excited Iron Complex with Nanosecond Lifetime. *Science* **2019**, *363* (6424), 249–253.

(11) Goswami, M.; Chirila, A.; Rebreyend, C.; de Bruin, B. EPR Spectroscopy as a Tool in Homogeneous Catalysis Research. *Top. Catal.* **2015**, *58* (12–13), 719–750.

(12) Williams, P. J. H.; Boustead, G. A.; Heard, D. E.; Seakins, P. W.; Rickard, A. R.; Chechik, V. New Approach to the Detection of Short-Lived Radical Intermediates. *J. Am. Chem. Soc.* **2022**, *144* (35), 15969–15976.

(13) Shaw, M. H.; Twilton, J.; MacMillan, D. W. C. Photoredox Catalysis in Organic Chemistry. *J. Org. Chem.* **2016**, *81* (16), 6898–6926.

(14) Bobo, M. V.; Kuchta, J. J.; Vannucci, A. K. Recent Advancements in the Development of Molecular Organic Photocatalysts. *Org. Biomol. Chem.* **2021**, *19* (22), 4816–4834.

(15) Srivastava, V.; Singh, P. P. Eosin Y Catalysed Photoredox Synthesis: A Review. *RSC Adv.* **2017**, *7* (50), 31377–31392.

(16) Nguyen, J. D.; D'Amato, E. M.; Narayanam, J. M. R.; Stephenson, C. R. J. Engaging Unactivated Alkyl, Alkenyl and Aryl Iodides in Visible-Light-Mediated Free Radical Reactions. *Nat. Chem.* **2012**, *4* (10), 854–859.

(17) Pirtsch, M.; Paria, S.; Matsuno, T.; Isobe, H.; Reiser, O. $[Cu(Dap)_2Cl]$ As an Efficient Visible-Light-Driven Photoredox Catalyst in Carbon–Carbon Bond-Forming Reactions. *Chem. – A Eur. J.* **2012**, *18* (24), 7336–7340.

(18) Herr, P.; Glaser, F.; Büldt, L. A.; Larsen, C. B.; Wenger, O. S. Long-Lived, Strongly Emissive, and Highly Reducing Excited States in Mo(0) Complexes with Chelating Isocyanides. *J. Am. Chem. Soc.* **2019**, *141* (36), 14394–14402.

(19) Fajardo, J.; Barth, A. T.; Morales, M.; Takase, M. K.; Winkler, J. R.; Gray, H. B. Photoredox Catalysis Mediated by Tungsten(0) Arylisocyanides. *J. Am. Chem. Soc.* **2021**, *143* (46), 19389–19398.

(20) Ravelli, D.; Protti, S.; Fagnoni, M. Carbon-Carbon Bond Forming Reactions via Photogenerated Intermediates. *Chem. Rev.* **2016**, *116* (17), 9850–9913.

(21) Kaufhold, S.; Wärnmark, K. Design and Synthesis of Photoactive Iron *N*-Heterocyclic Carbene Complexes. *Catalysts* **2020**, *10* (1), 132.

(22) Juban, E. A.; Smeigh, A. L.; Monat, J. E.; McCusker, J. K. Ultrafast Dynamics of Ligand-Field Excited States. *Coord. Chem. Rev.* **2006**, *250* (13–14), 1783–1791.

(23) Fredin, L. A.; Pápai, M.; Rozsályi, E.; Vankó, G.; Wärnmark, K.; Sundström, V.; Persson, P. Exceptional Excited-State Lifetime of an Iron(II)–*N*-Heterocyclic Carbene Complex Explained. *J. Phys. Chem. Lett.* **2014**, *5* (12), 2066–2071.

(24) Liu, Y.; Persson, P.; Sundström, V.; Wärnmark, K. Fe *N*-Heterocyclic Carbene Complexes as Promising Photosensitizers. *Acc. Chem. Res.* **2016**, *49* (8), 1477–1485.

(25) Wenger, O. S. Is Iron the New Ruthenium? *Chem. – A Eur. J.* **2019**, *25* (24), 6043–6052.

(26) Liu, Y.; Harlang, T.; Canton, S. E.; Chábera, P.; Suárez-Alcántara, K.; Fleckhaus, A.; Vithanage, D. A.; Göransson, E.; Corani, A.; Lomoth, R.; Sundström, V.; Wärnmark, K. Towards Longer-Lived Metal-to-Ligand Charge Transfer States of Iron(II) Complexes: An *N*-Heterocyclic Carbene Approach. *Chem. Commun.* **2013**, *49* (57), 6412–6414.

(27) Chábera, P.; Liu, Y.; Prakash, O.; Thyrhaug, E.; Nahhas, A. El; Honarfar, A.; Essén, S.; Fredin, L. A.; Harlang, T. C. B.; Kjær, K. S.; Handrup, K.; Ericson, F.; Tatsuno, H.; Morgan, K.; Schnadt, J.; Häggström, L.; Ericsson, T.; Sobkowiak, A.; Lidin, S.; Huang, P.; Styring, S.; Uhlig, J.; Bendix, J.; Lomoth, R.; Sundström, V.; Persson, P.; Wärnmark, K. A Low-Spin Fe(III) Complex with 100-Ps Ligand-to-Metal Charge Transfer Photoluminescence. *Nature* **2017**, *543* (7647), 695–699.

(28) Chábera, P.; Kjaer, K. S.; Prakash, O.; Honarfar, A.; Liu, Y.; Fredin, L. A.; Harlang, T. C. B.; Lidin, S.; Uhlig, J.; Sundström, V.; Lomoth, R.; Persson, P.; Wärnmark, K. Fe^{II} Hexa *N*-Heterocyclic Carbene Complex with a 528 Ps Metal-to-Ligand Charge-Transfer Excited-State Lifetime. *J. Phys. Chem. Lett.* **2018**, *9* (3), 459–463.

(29) Young, E. R.; Oldacre, A. Iron Hits the Mark. *Science* **2019**, *363* (6424), 225–226.

(30) Kharasch, M. S.; Jensen, E. V.; Urry, W. H. Addition of Carbon Tetrachloride and Chloroform to Olefins. *Science* **1945**, *102* (2640), 128–128.

(31) Kharasch, M. S.; Urry, W. H.; Jensen, E. V. Addition of Derivatives of Chlorinated Acetic Acids to Olefins. *J. Am. Chem. Soc.* **1945**, *67* (9), 1626.

(32) Kharasch, M. S.; Skell, P. S.; Fisher, P. Reactions of Atoms and Free Radicals in Solution. XII. The Addition of Bromo Esters to Olefins. *J. Am. Chem. Soc.* **1948**, *70* (3), 1055–1059.

(33) Curran, D. P.; Chen, M. H.; Spletzer, E.; Seong, C. M.; Chang, C. T. Atom-Transfer Addition and Annulation Reactions of Iodomalonates. *J. Am. Chem. Soc.* **1989**, *111* (24), 8872–8878.

(34) Baciocchi, E.; Muraglia, E. Synthesis of γ-Haloesters and γ-Ketoesters by Homolytic Addition of Carbon Radicals Generated by α-Haloesters and Triethylborane to Alkenes and Silyl Enol Ethers. *Tetrahedron Lett.* **1994**, *35* (17), 2763–2766.

(35) Iqbal, J.; Bhatia, B.; Nayyar, N. K. Transition Metal-Promoted Free-Radical Reactions in Organic Synthesis: The Formation of Carbon-Carbon Bonds. *Chem. Rev.* **1994**, *94* (2), 519–564.

(36) Gossage, R. A.; van de Kuil, L. A.; van Koten, G. Diaminoarylnickel(II) "Pincer" Complexes: Mechanistic Considerations in the Kharasch Addition Reaction, Controlled Polymerization, and Dendrimeric Transition Metal Catalysts. *Acc. Chem. Res.* **1998**, *31* (7), 423–431.

(37) Pintauer, T.; Matyjaszewski, K. Atom Transfer Radical Addition and Polymerization Reactions Catalyzed by Ppm Amounts of Copper Complexes. *Chem. Soc. Rev.* **2008**, *37* (6), 1087–1097.

(38) Muñoz-Molina, J. M.; Belderrain, T. R.; Pérez, P. J. Atom Transfer Radical Reactions as a Tool for Olefin Functionalization – On the Way to Practical Applications. *Eur. J. Inorg. Chem.* **2011**, *2011* (21), 3155–3164.

(39) Curran, D. P. Fluorous Reverse Phase Silia Gel. A New Tool for Preparative Separations in Synthetic Organic and Organofluorine Chemistry. *Synlett* **2001**, *2001* (09), 1488–1496.

(40) Engl, S.; Reiser, O. Copper-Photocatalyzed ATRA Reactions: Concepts, Applications, and Opportunities. *Chem. Soc. Rev.* **2022**, *51* (13), 5287–5299.

(41) Wallentin, C.-J. J.; Nguyen, J. D.; Finkbeiner, P.; Stephenson, C. R. J. Visible Light-Mediated Atom Transfer Radical Addition via Oxidative and Reductive Quenching of Photocatalysts. *J. Am. Chem. Soc.* **2012**, *134* (21), 8875–8884.

(42) Nguyen, J. D.; Tucker, J. W.; Konieczynska, M. D.; Stephenson, C. R. J. Intermolecular Atom Transfer Radical Addition to Olefins Mediated by Oxidative Quenching of Photoredox Catalysts. *J. Am. Chem. Soc.* **2011**, *133* (12), 4160–4163.

(43) Lowry, M. S.; Goldsmith, J. I.; Slinker, J. D.; Rohl, R.; Pascal, R. A.; Malliaras, G. G.; Bernhard, S. Single-Layer Electroluminescent Devices and Photoinduced Hydrogen Production from an Ionic Iridium(III) Complex. *Chem. Mater.* **2005**, *17* (23), 5712–5719.

(44) Lowry, M. S.; Goldsmith, J. I.; Slinker, J. D.; Pascal, R. A.; Malliaras, G. G.; Bernhard, S. Correction to Single-Layer Electroluminescent Devices and Photoinduced Hydrogen Production from an Ionic Iridium(III) Complex. *Chem. Mater.* **2023**, *35* (3), 1466–1466.

(45) Pavlishchuk, V. V.; Addison, A. W. Conversion Constants for Redox Potentials Measured versus Different Reference Electrodes in Acetonitrile Solutions at 25°C. *Inorganica Chim. Acta* **2000**, *298* (1), 97–102.

(46) Roth, H.; Romero, N.; Nicewicz, D. Experimental and Calculated Electrochemical Potentials of Common Organic Molecules for Applications to Single-Electron Redox Chemistry. *Synlett* **2015**, *27* (05), 714–723.

(47) Tu, Y.-J.; Njus, D.; Schlegel, H. B. A Theoretical Study of Ascorbic Acid Oxidation and $HOO^{\cdot}/O_2^{\cdot-}$ Radical Scavenging. *Org. Biomol. Chem.* **2017**, *15* (20), 4417–4431.

(48) Hepatochem web page https://www.hepatochem.com/photoreactors-leds-accessories/photoredox-box/ (accessed 2023 -09 -01).

(49) Pan, X.; Malhotra, N.; Zhang, J.; Matyjaszewski, K. Photoinduced Fe-Based Atom Transfer Radical Polymerization in the Absence of Additional Ligands, Reducing Agents, and Radical Initiators. *Macromolecules* **2015**, *48* (19), 6948–6954.

(50) HK Testsysteme GmbH web page http://wppr.photoreactor.de/how-to-use/ (accessed 2023 -09 -01).

(51) Pellegrin, Y.; Odobel, F. Sacrificial Electron Donor Reagents for Solar Fuel Production. *Comptes Rendus Chim.* **2017**, *20* (3), 283–295.

(52) Rosemann, N. W.; Chábera, P.; Prakash, O.; Kaufhold, S.; Wärnmark, K.; Yartsev, A.; Persson, P. Tracing the Full Bimolecular Photocycle of Iron(III)–Carbene Light Harvesters in Electron-Donating Solvents. *J. Am. Chem. Soc.* **2020**, *142* (19), 8565–8569.

(53) Aydogan, A.; Bangle, R. E.; De Kreijger, S.; Dickenson, J. C.; Singleton, M. L.; Cauët, E.; Cadranel, A.; Meyer, G. J.; Elias, B.; Sampaio, R. N.; Troian-Gautier, L. Mechanistic Investigation of a Visible Light Mediated Dehalogenation/Cyclisation Reaction Using Iron(III), Iridium(III) and Ruthenium(II) Photosensitizers. *Catal. Sci. Technol.* **2021**, *11* (24), 8037–8051.

(54) Aydogan, A.; Bangle, R. E.; Cadranel, A.; Turlington, M. D.; Conroy, D. T.; Cauët, E.; Singleton, M. L.; Meyer, G. J.; Sampaio, R. N.; Elias, B.; Troian-Gautier, L. Accessing Photoredox Transformations with an Iron(III) Photosensitizer and Green Light. *J. Am. Chem. Soc.* **2021**, *143* (38), 15661–15673.

(55) Wang, Y.; Suzuki, H.; Xie, J.; Tomita, O.; Martin, D. J.; Higashi, M.; Kong, D.; Abe, R.; Tang, J. Mimicking Natural Photosynthesis: Solar to Renewable H_2 Fuel Synthesis by Z-Scheme Water Splitting Systems. *Chem. Rev.* **2018**, *118* (10), 5201–5241.

(56) Qiao, Y.; Yang, Q.; Schelter, E. J. Photoinduced Miyaura Borylation by a Rare-Earth-Metal Photoreductant: The Hexachlorocerate(III) Anion. *Angew. Chemie Int. Ed.* **2018**, *57* (34), 10999–11003.

(57) Pitre, S. P.; McTiernan, C. D.; Vine, W.; DiPucchio, R.; Grenier, M.; Scaiano, J. C. Visible-Light Actinometry and Intermittent Illumination as Convenient Tools to Study $Ru(Bpy)_3Cl_2$ Mediated Photoredox Transformations. *Sci. Rep.* **2015**, *5* (1), 16397.

(58) Rabani, J.; Mamane, H.; Pousty, D.; Bolton, J. R. Practical Chemical Actinometry—A Review. *Photochem. Photobiol.* **2021**, *97* (5), 873–902.

(59) Andrieux, C. P.; Gelis, L.; Medebielle, M.; Pinson, J.; Saveant, J. M. Outer-Sphere Dissociative Electron Transfer to Organic Molecules: A Source of Radicals or Carbanions? Direct and Indirect Electrochemistry of Perfluoroalkyl Bromides and Iodides. *J. Am. Chem. Soc.* **1990**, *112* (9), 3509–3520.

(60) Budén, M. E.; Guastavino, J. F.; Rossi, R. A. Room-Temperature Photoinduced Direct C-H-Arylation via Base-Promoted Homolytic Aromatic Substitution. *Org. Lett.* **2013**, *15* (6), 1174–1177.

(61) Studer, A.; Curran, D. P. Organocatalysis and C-H Activation Meet Radical- and Electron-Transfer Reactions. *Angew. Chemie - Int. Ed.* **2011**, *50* (22), 5018–5022.

(62) Pratap, R.; Ram, V. J. Natural and Synthetic Chromenes, Fused Chromenes, and Versatility of Dihydrobenzo[*h*]Chromenes in Organic Synthesis. *Chem. Rev.* **2014**, *114* (20), 10476–10526.

(63) Cui, H.-L. Recent Progress in the Synthesis of Pyrrolo[2,1-*a*]Isoquinolines. *Org. Biomol. Chem.* **2022**, *20* (14), 2779–2801.

(64) Ghosh, I.; Ghosh, T.; Bardagi, J. I.; König, B. Reduction of Aryl Halides by Consecutive Visible Light-Induced Electron Transfer Processes. *Science* **2014**, *346* (6210), 725–728.

(65) Constantin, T.; Juliá, F.; Sheikh, N. S.; Leonori, D. A Case of Chain Propagation: α-Aminoalkyl Radicals as Initiators for Aryl Radical Chemistry. *Chem. Sci.* **2020**, *11* (47), 12822–12828.

(66) Constantin, T.; Zanini, M.; Regni, A.; Sheikh, N. S.; Juliá, F.; Leonori, D. Aminoalkyl Radicals as Halogen-Atom Transfer Agents for Activation of Alkyl and Aryl Halides. *Science* **2020**, *367* (6481), 1021–1026.

(67) Pause, L.; Robert, M.; Savéant, J.-M. Can Single-Electron Transfer Break an Aromatic Carbon−Heteroatom Bond in One Step? A Novel Example of Transition between Stepwise and Concerted Mechanisms in the Reduction of Aromatic Iodides. *J. Am. Chem. Soc.* **1999**, *121* (30), 7158–7159.

(68) Heredia, M. D.; Puiatti, M.; Rossi, R. A.; Budén, M. E. Visible Light Mediated Synthesis of 6*H*-Benzo[*c*]Chromenes: Transition-Metal-Free Intramolecular Direct C-H Arylation. *Org. Biomol. Chem.* **2022**, *20* (1), 228–239.

(69) Danen, W. C.; Saunders, D. G.; Rose, K. A. Halogen Abstraction Studies. V. Abstraction of Iodine by Phenyl Radicals from Iodonaphthalenes, Iodopyridines, and Iodothiophenes. Question of Polar Effects. *J. Am. Chem. Soc.* **1974**, *96* (14), 4558–4562.

(70) Graeve, R.; Wahl, G. H. Kugelrohr Distillation Apparatus. *J. Chem. Educ.* **1964**, *41* (5), 279.

(71) Prakash, O.; Chábera, P.; Rosemann, N. W.; Huang, P.; Häggström, L.; Ericsson, T.; Strand, D.; Persson, P.; Bendix, J.; Lomoth, R.; Wärnmark, K. A Stable Homoleptic Organometallic Iron(IV) Complex. *Chem. – A Eur. J.* **2020**, *26* (56), 12728–12732.

(72) Beatty, J. W.; Stephenson, C. R. J. Amine Functionalization via Oxidative Photoredox Catalysis: Methodology Development and Complex Molecule Synthesis. *Acc. Chem. Res.* **2015**, *48* (5), 1474–1484.

(73) Wood, M. E.; Bissiriou, S.; Lowe, C.; Norrish, A. M.; Sénéchal, K.; Windeatt, K. M.; Coles, S. J.; Hursthouse, M. B. Synthetic Use of the Primary Kinetic Isotope Effect in Hydrogen Atom Transfer: Generation of α-Aminoalkyl Radicals. *Org. Biomol. Chem.* **2010**, *8* (20), 4653–4665.

(74) More, S. A.; Kardile, R. D.; Kuo, T.-C.; Cheng, M.-J.; Liu, R.-S. Gold Catalysts Can Generate Nitrone Intermediates from a Nitrosoarene/Alkene Mixture, Enabling Two Distinct Catalytic Reactions: A Nitroso-Activated Cycloheptatriene/Benzylidene Rearrangement. *Org. Lett.* **2021**, *23* (14), 5506–5511.

(75) Cong, X.; Tang, H.; Zeng, X. Regio- and Chemoselective Kumada–Tamao–Corriu Reaction of Aryl Alkyl Ethers Catalyzed by Chromium Under Mild Conditions. *J. Am. Chem. Soc.* **2015**, *137* (45), 14367–14372.

(76) Yao, Q. J.; Zhang, S.; Zhan, B. B.; Shi, B. F. Atroposelective Synthesis of Axially Chiral Biaryls by Palladium-Catalyzed Asymmetric C−H Olefination Enabled by a Transient Chiral Auxiliary. *Angew. Chemie - Int. Ed.* **2017**, *56* (23), 6617–6621.

(77) Péter, Á.; Agasti, S.; Knowles, O.; Pye, E.; Procter, D. J. Recent Advances in the Chemistry of Ketyl Radicals. *Chem. Soc. Rev.* **2021**, *50* (9), 5349–5365.

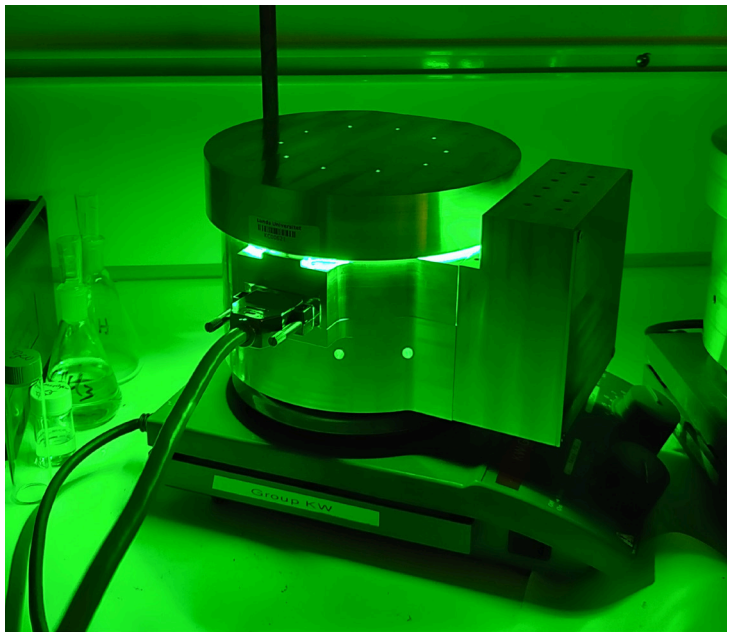

Printed by Media-Tryck, Lund 2021 NORDIC SWAN ECOLABEL 3041 0903

LUND UNIVERSITY

ISBN 978-91-8096-000-7

Centre for Analysis and Synthesis
Department of Chemistry
Faculty of Science
Lund University